The Astrophysical Journal, 858:68 (26pp), 2018 May 10 https://doi.org/10.3847/1538-4357/aabbac

Swift Observations of Mrk 421 in Selected Epochs. II. An Extreme Spectral Flux Variability in 2009–2012

B. Kapanadze[1,2], S. Vercellone[2], P. Romano[2], P. Hughes[3], M. Aller[3], H. Aller[3], O. Kharshiladze[4], and L. Tabagari[1]
[1] E. Kharadze Abastumani Astrophysical Observatory, Ilia State University, Colokashvili Av. 3/5, Tbilisi, 0162, Georgia
[2] INAF, Osservatorio Astronomico di Brera, Via E. Bianchi 46, I-23807 Merate, Italy
[3] Astronomy Department, University of Michigan, Ann Arbor, MI 48109-1107, USA
[4] Department of Physics, I. Javaksishvili State University, Chavchavadze Av. 3, Tbilisi 0128, Republic of Georgia
Received 2018 January 31; revised 2018 March 25; accepted 2018 March 29; published 2018 May 7

Abstract

We present the results from a detailed spectral and timing study of Mrk 421 based on the rich archival *Swift* data obtained during 2009–2012. Best fits of the 0.3–10 keV spectra were mostly obtained using the log-parabolic model showing the relatively low spectral curvature that is expected in the case of efficient stochastic acceleration of particles. The position of the synchrotron spectral energy density peak E_p of 173 spectra is found at energies higher than 2 keV. The photon index at 1 keV exhibited a very broad range of values $a = 1.51$–3.02, and very hard spectra with $a < 1.7$ were observed during the strong X-ray flares, hinting at a possible hadronic jet component. The spectral parameters varied on diverse timescales and showed a correlation in some periods, which is expected in the case of first- and second-order Fermi acceleration. The 0.3–10 keV flux showed strong X-ray flaring activity by a factor of 3–17 on timescales of a few days–weeks between the lowest historical state and that corresponding to a rate higher than 100 cts s^{-1}. Moreover, 113 instances of intraday variability were revealed, exhibiting shortest flux-doubling/halving times of about 1.2 hr, as well as brightenings by 7%–24% in 180–720 s and declines by 68%–22% in 180–900 s. The X-ray and very high-energy fluxes generally showed a correlated variability, although one incidence of a more complicated variability was also detected, indicating that the multifrequency emission of Mrk 421 could not be generated in a single zone.

Key words: BL Lacertae objects: individual (Mrk 421)

Supporting material: machine-readable tables

1. Introduction

The active galactic nucleus (AGN) Mrk 421 represents one of the most extreme representative BL Lacertae objects (BLLs), which are characterized by the absence of emission lines, strong flux variability in almost all spectral bands, compact radio-structure, superluminal motion of some components, and very broad continuum extending from the radio to the very high-energy γ-rays ($E > 100$ GeV) that makes BLLs the most frequently detected class of the extragalactic TeV sources[5] (see Falomo et al. 2014). Note that Mrk 421 was the first TeV-detected extragalactic source (Punch et al. 1992), making this object a frequent target of multiwavelength (MWL) campaigns (Macomb et al. 1995; Fossati et al. 2008; Acciari et al. 2009; Alecsic et al. 2015a; Balocovic et al. 2016 etc.).

The aforementioned BLL features are commonly interpreted as being due to the beamed, nonthermal emission from a relativistic jet that is closely aligned to our line of sight (Urry & Padovani 1995, and references therein). The broadband spectral energy distribution (SED) of BLLs shows a double-humped shape in the ν–νF_ν plane. Owing to the polarized emission observed in the frequency range of the lower-energy SED component (from radio to UV–X-ray frequencies), its origin is widely accepted to be produced by a distribution of relativistic electrons. Based on the position of the synchrotron SED peak E_p, BLLs are divided into two subclasses (Padovani & Giommi 1995 and references therein): high-energy-peaked objects (HBLs, peaking at UV–X-ray frequencies), and low–peaked objects (LBLs, with E_p situated in the infrared–optical part of the spectrum). However, many details related to the particle acceleration and cooling that are related to the origin and nature of powerful, non-stationary processes in the innermost AGN area are still under debate.

On the other hand, there is a variety of models developed for the explanation of the origin of the SED higher-energy component: (1) an inverse-Compton (IC) scattering of synchrotron photons by their "parent" electron–positron population (so-called synchrotron self-Compton model, SSC; Marscher & Gear 1985); (2) hadronic models incorporating a production of γ-rays by relativistic protons, either directly (synchrotron proton blazar model; Abdo et al. 2011) or indirectly (e.g., synchrotron from a second electron population produced by a cascade induced by the interaction of high-energy protons with ambient photons; Mannheim 1993). A valid model can be discerned via the intense MWL flux variability and interband cross-correlation study, which also provides important clues about underlying physical processes, the structure, and the dynamics of the emission zone.

Kapanadze et al. (2018; hereafter Paper I) presented the results of a detailed study of X-ray spectral and flux variability in the MWL context, focussed on the rich archival data obtained with the X-ray telescope (XRT, Burrows et al. 2005) on board *Swift* (Gehrels et al. 2004) during 2005 March–2008 June. In this paper, we present the second part of this study, based on the *Swift* observations of Mrk 421 performed in 2009 January–2012 December. Although a part of these observations was included in published papers (see Alecsic et al. 2015a, 2015b; Ahnen et al. 2016), a high X-ray brightness of the source and excellent instrumental capabilities of

[5] http://tevcat.uchicago.edu/

Table 1
Summary of the XRT and UVOT Observations in 2005 March–2008 June (Extract; See the Corresponding Machine-readable Table for the Full Version)

ObsID	Obs. Start–End (UTC)	Expos. (s)	CR (cts s^{-1})	UVW1 (mag)	UVW1 (mJy)	UVM2 (mag)	UVM2 (mJy)	UVW2 (mag)	UVW2 (mJy)
(1)	(2)	(3)	(4)	(5)	(6)	(7)	(8)	(9)	(10)
30352104	2009 Jan 12 19:20:47 01–12 23:29:01	794	34.47(0.18)	12.02(0.04)	13.84(0.52)	12.66(0.04)	6.61(0.17)	12.01(0.03)	9.09(0.21)
30352105	2009 Jan 13 17:40:00 01–13 18:41:53	770	34.47(0.23)	12.07(0.04)	13.21(0.42)	12.72(0.04)	6.27(0.12)	12.06(0.03)	8.71(0.20)
30352106	2009 Jan 18 00:19:00 01–18 02:58:56	1089	32.67(0.23)	12.25(0.03)	11.18(0.35)	12.89(0.04)	5.37(0.13)	12.15(0.03)	7.99(0.19)
30352107	2009 Jan 27 12:11:00 01–27 14:47:26	929	33.84(0.26)	12.29(0.03)	10.77(0.34)	12.94(0.04)	5.11(0.10)	12.28(0.03)	7.14(0.17)

Note. The columns are as follows: (1)—Observation ID; (2)—Observation start–end; (3)—Exposure (in seconds); (4) Observation-binned Count Rate (CR) with its error; (5)–(10)—De-reddened UVOT magnitudes and fluxes.

(This table is available in its entirety in machine-readable form.)

Swift–XRT (good photon statistics and low background counts) allow us to perform a detailed study of X-ray spectral and flux variability on various timescales, down to a few hundred seconds. Note that Alecsic et al. (2015a, 2015b) and Ahnen et al. (2016) mostly focussed on TeV-band variability of the source, searching for the MWL correlations and SED modeling, and no detailed X-ray spectral and flux variability studies were performed. A significant part of *Swift* observations in 2009–2012 of our target have not been included in any published papers, and they may contribute to the understanding of extreme flux and spectral variability of this BLL. Using the XRT observations, we checked a correlation of the 0.3–10 keV flux variability with the simultaneous MWL fluxes obtained with different instruments: the Ultraviolet-Optical Telescope (UVOT; Roming et al. 2005) and Burst Alert Telescope (BAT; Barthelmy et al. 2005) on board *Swift*, the Large Area Telescope (LAT) on board *Fermi*; Atwood et al. 2009), and ground-based Cherenkov-type, optical and radio telescopes.

The paper is organized as follows. Section 2 describes the data processing and analyzing procedures. In Section 3, we provide the results of a spectral analysis. Those related to the MWL flux and spectral variability on diverse timescales are presented in Section 4. We discuss our results and provide our conclusions in Section 5.

2. Observations and Data Reduction

The source was observed 370 times by the XRT between 2009 January 12 and 2012 December 30 with a total exposure of 403.6 ks. The information about each pointing and the corresponding count rates is provided in Table 1,[6] which also contains the results from the simultaneous UVOT observations in the ultraviolet bands UVW1, UVM2, and UVW2 (deabsorbed magnitudes and corresponding fluxes in milli-Jansky). The XRT and UVOT data were processed using the recipes described in Paper I.

We extracted the 0.3–300 GeV fluxes from the LAT observations using the events of the diffuse class from a region of interest (ROI) of radius 10°, centered on Mrk 421, and processed with the `Science Tools` package (version v10r0p5) and P8R2_V6 instrument response function using the unbinned maximum likelihood method `GTLIKE`. In order to greatly reduce contamination from Earth limb photons, we have excluded events at zenith angles >100° and any events recorded when the spacecraft rocking angle was larger than 52°. A background model including all γ-ray sources from the *Fermi*-LAT four-year Point Source Catalog (3FGL, Acero et al. 2015) within 20° of Mrk 421 was created. For the spectral modeling of Mrk 421, we adopted a simple power law, as was done in the 3FGL catalog. The spectral parameters of sources within the ROI were left free during the minimization process, while those outside of this range were held fixed to the 3FGL catalog values. The Galactic and extragalactic diffuse γ-ray emission as well as the residual instrumental background are included using the recommended model files `gll_iem_v06.fits` and `iso_P8R2_SOURCE_V6_v06.txt`. The normalizations of both components in the background model were allowed to vary freely during the spectral fit.

3. Spectral Analysis

We extracted the 0.3–10 keV spectra using the `XSPEC` package and fitted them with the models that are generally applicable for blazar X-ray spectra[7]: simple or broken power laws, and the log-parabolic model (see Paper I for a description, as well as for the details of the spectral reduction and derivation of deabsorbed 0.3–2, 2–10, and 0.3–10 keV fluxes). We generated the spectra from separate orbits of the particular ObsID when it was impossible to use the same source and/or background extraction regions for all orbits, or when the source showed a flux variability during this observation. In each case, the model validity was checked by means of the reduced chi-squared (χ^2_r), distribution of the residuals and the F-test. Moreover, we extracted the spectra even from the segments of the particular orbit when the flux varied within it (especially in flaring X-ray states), or when there was no satisfactory value of χ^2_r (between 0.9 and 1.1) for the spectrum extracted from the whole orbit.

For the vast majority of the 0.3–10 keV spectra (851 out of 912), simple or broken power-law models were excluded at the 99.99% confidence level, and the log-parabolic model was clearly preferred by the aforementioned tests. The corresponding results (the values of the photon index at 1 keV, curvature parameter, position of the SED peak, deabsorbed

[6] The three leading zeroes in observation IDs are omitted everywhere in the paper.

[7] The hydrogen column density was fixed to the Galactic value $N_H = 1.90 \times 10^{20}$ cm^{-2} (Kalberla et al. 2005).

Table 2
Results of the Spectral Analysis with the log-parabolic Model (Extract; See the Corresponding Machine-readable Table for the Full Version)

ObsId (1)	a (2)	b (3)	E_p (4)	$10 \times K$ (5)	χ^2/d.o.f. (6)	$\log F_{0.3-2\,\mathrm{keV}}$ (7)	$\log F_{2-10\,\mathrm{keV}}$ (8)	$\log F_{0.3-10\,\mathrm{keV}}$ (9)	HR (10)
30352104 Or1	2.01(0.02)	0.29(0.05)	0.96(0.09)	22(0.03)	1.16/219	−9.23(0.01)	−9.42(0.02)	−9.01(0.01)	0.65(0.02)
30352104 Or2	1.98(0.02)	0.34(0.04)	1.07(0.09)	2.21(0.)	0.93/275	−9.20(0.01)	−9.38(0.01)	−8.98(0.01)	0.66(0.02)
30352105 S1(380 s)	2.05(0.02)	0.25(0.05)	0.79(0.08)	26(0.02)	1.08/247	−9.22(0.01)	−9.41(0.01)	−9.00(0.01)	0.63(0.02)
30352105 S2(380 s)	2.07(0.02)	0.21(0.05)	0.68(0.07)	2.04(0.02)	1.06/244	−9.22(0.01)	−9.42(0.01)	−9.00(0.01)	0.63(0.02)

Note. The E_p values (Column 4) are given in keV; unabsorbed 0.3–2, 2–10, and 0.3–10 keV fluxes (Columns 7–9)—in erg cm^{-2} s^{-1}.
(This table is available in its entirety in machine-readable form.)

fluxes, and the hardness ratio calculated as HR $= F_{2-10\,\mathrm{keV}}/F_{0.3-2\,\mathrm{keV}}$, where the quantities $F_{2-10\,\mathrm{keV}}$ and $F_{0.3-2\,\mathrm{keV}}$ stand for the unabsorbed 2–10 keV to 0.3–2 keV fluxes, respectively) are provided in Table 2.

In Table 3, we present the properties of the distribution of the a, HR, and b parameters for the whole 2009–2012 period and for its separate parts (Periods 1–6, selected depending on the occurrence of enhanced X-ray activity of Mrk 421 or intensive XRT campaigns).

3.1. Photon Index

The photon index at 1 keV showed a very wide range of values in 2009–2012: $\Delta a = 1.51$ with the hardest value of $a = 1.51 \pm 0.02$ (derived from the second 107 s segment of the second orbit of ObsID 30352155, MJD 55147.8). Note that this is the lowest value of the parameter a from the XRT observations of Mrk 421 during 2005–2015, and 362 spectra were harder than $a = 2$ (43% of all log-parabolic spectra). Note that this percentage is smaller than in 2005–2008 (46%; Paper I) and larger than those shown in the periods 2013 January–May and 2013 November–2015 June (20–39%; see Kapanadze et al. 2016a, 2017a).

Of the spectra with $a < 2$, 49% showed $a \leqslant 1.86$ (corresponding to $E_p \gtrsim 2$ keV for the most frequent value of the curvature parameter $b = 0.23$ during 2009–2012), and 27 spectra (7.5%) were very hard, corresponding to $a < 1.7$ (see Section 5.2 for the corresponding physical implication). Of the spectra with $a \geqslant 2$, 58% are softer than $a = 2.24$ (corresponding to $E_p < 0.3$ keV for the aforementioned value of the parameter b, i.e., the presence of the synchrotron SED peak beyond the instrumental range of XRT), and 30% show $a > 2.46$ (corresponding to $E_p < 0.1$ keV, a conventional lower-energy threshold for X-rays).

On average, Period 3 was notable with the hardest spectra of the different periods in 2009–2012, with the mean value $\overline{a} = 1.87$. Eighty-two percent of the spectra show $a < 2$, and seven spectra with $a < 1.7$ belong to this period (Figure 1(Ac)). Although Period 2 was characterized by the majority of very hard spectra (20 out of 27), it contained significantly lower percentage of the spectra with $a < 2$ and they had a higher mean value as well as negative skewness, indicating a shift of the corresponding distribution toward higher values with respect to $\overline{a}$ (see Table 3 and Figure 1(Ab)). In contrast, Period 5 showed the softest spectra: the spectrum with the highest historical value of the photon index $a_{\mathrm{max}} = 3.02 \pm 0.06$, derived from ObsID 31202082 (MJD 55606.2), belongs to this period. Ninety-eight percent of the spectra from this period show a synchrotron SED peak beyond the instrumental range of the XRT, and their majority (73%) are UV-peaking spectra (see Figure 1(Ai)).

Table 3
Distribution of Spectral Parameters in Different Periods: Minimum and Maximum Values (Columns 2 and 3, Respectively), Mean Value (Column 4), and Skewness (Last Column)

Par. (1)	Min. (2)	Max. (3)	Mean (4)	Skewness (5)
2009–2012				
a	1.51	3.02	2.13	0.49
b	0.09	0.64	0.27	0.77
E_p	0.80	7.94	2.20	1.94
Γ	1.75	2.93	2.31	−0.21
HR	0.11	1.47	0.62	0.45
Period 1 2009 Jan 12–May 27				
a	1.98	2.59	2.28	0.05
b	0.14	0.47	0.27	0.48
E_p	0.80	7.94	3.04	0.72
HR	0.26	0.68	0.44	0.33
Period 2 2009 Nov 12–2010 Jan 31				
a	1.51	2.54	1.95	−0.32
b	0.09	0.64	0.30	0.69
E_p	0.81	...	1.44	4.98
HR	0.29	1.47	0.74	1.27
Period 3 2010 Feb 1–Apr 13				
a	1.66	2.47	1.90	1.17
b	0.11	0.41	0.23	0.42
E_p	0.80	7.81	2.57	1.65
HR	0.302	1.31	0.88	0.04
Period 4 2010 Apr 13–Jul 14				
a	1.71	2.65	2.06	0.70
b	0.10	0.47	0.23	0.46
E_p	0.80	7.81	1.98	1.36
HR	0.23	1.30	0.81	−0.38
Period 5 2010 Dec 3–2011 Jun 10				
a	2.23	3.02	2.57	0.13
b	0.14	0.57	0.31	0.53
HR	0.11	0.46	0.26	0.43
Period 6 2011 Oct 5–2012 May 31				
a	2.14	2.91	2.48	0.14
b	0.12	0.48	0.28	0.25
HR	0.14	0.62	0.32	0.62

Period 6 was also characterized by one of the softest spectra during 2009–2012: 93% show a synchrotron peak beyond the XRT instrumental range (Figure 1(Ae)), and 51% of the E_p

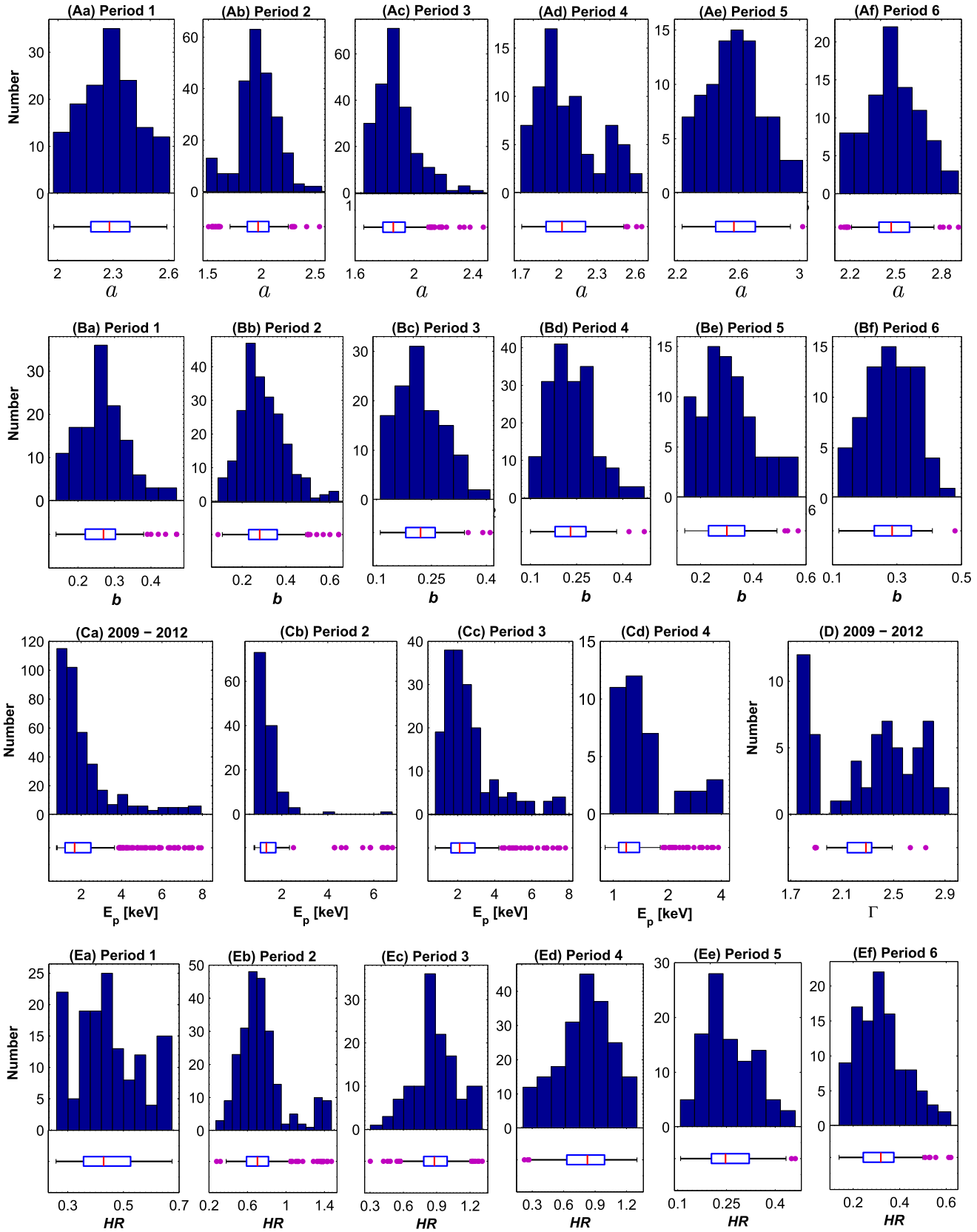

Figure 1. Distribution of the spectral parameter values in different periods. The red line within each box-plot corresponds to the median of the distribution, and the purple points represent the outliers.

values belong to the UV band. The corresponding mean value ($\overline{a} = 2.48$) is only 4% lower than its "counterpart" in Period 5 (see Table 3). The spectra extracted from the XRT observations in 2012 November–December, which are not included in any period, are also very soft: $a = 2.53$–2.92, and the mean value is $\overline{a} = 2.71$.

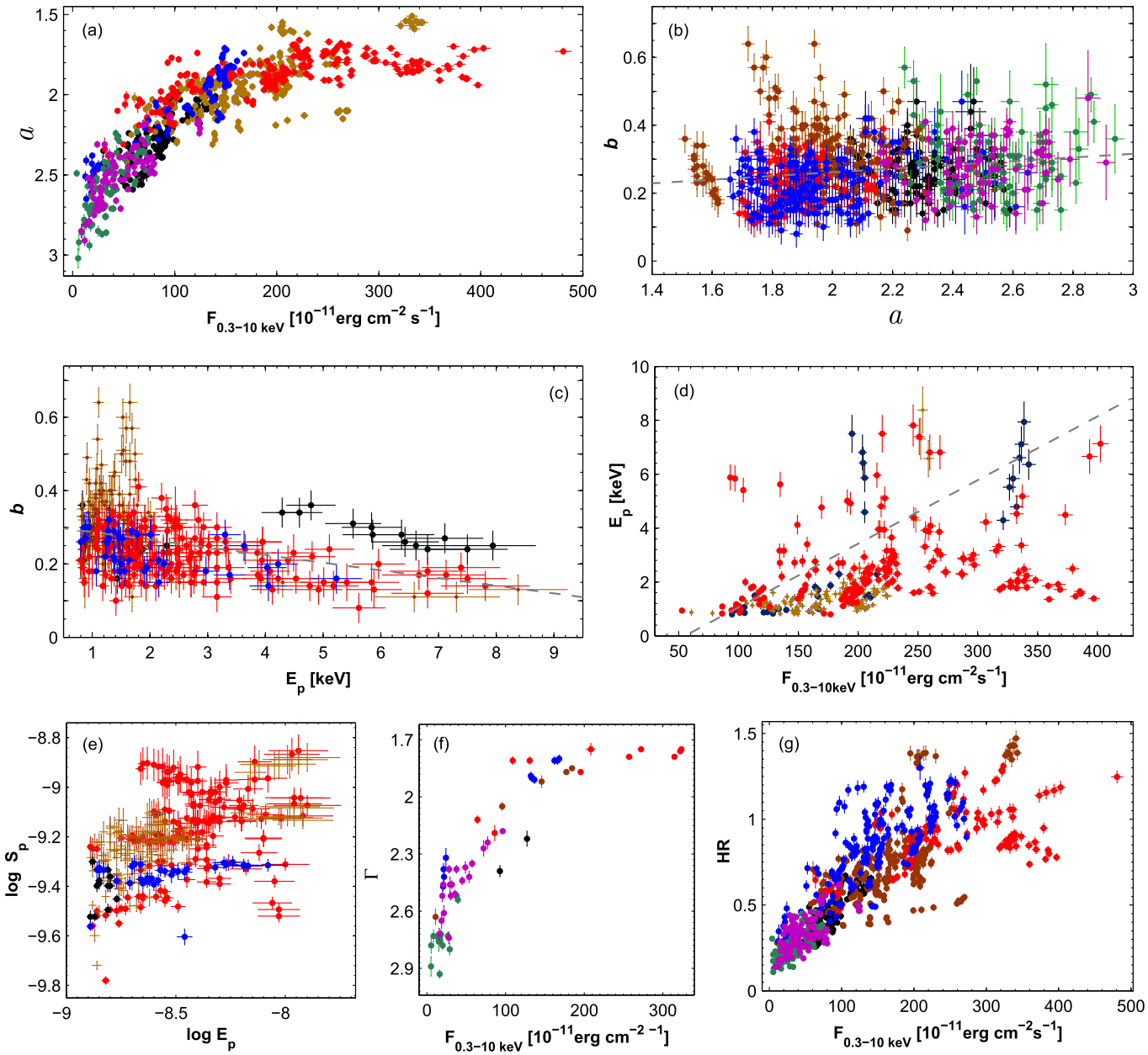

Figure 2. Correlation between the spectral parameters and fluxes. The colored points in Figures 2(a)–(h) correspond to the different periods as follows: black—Period 1, brown—Period 2. red—Period 3, blue—Period 4, green—Period 5, and purple—Period 6. Gray dashed lines represent linear fits to the scatter plots.

Figure 2(a) shows an anticorrelation between the parameter a and 0.3–10 keV flux (see Figure 2(a) and Table 4 for the Spearman coefficient ρ and corresponding p-value), implying that the source mostly followed a "harder-when-brighter" trend during 2009–2012. In fact, the aforementioned highest historical value of the photon index corresponds to one of the lowest historical 0.3–10 keV fluxes of 5.4×10^{-11} erg cm^{-2} s^{-1}, while the flux derived from the hardest spectrum is higher by a factor of 61.5 than this value. The same figure shows that this trend was strongest in Periods 1 and 4, while the anticorrelation a–$F_{0.3\text{–}10\,\mathrm{keV}}$ was relatively weaker in Periods 2–3 (see Table 4), and the sub-samples from these periods, corresponding to the highest X-ray states, do not follow the general trend.

3.2. Curvature Parameter and the Position of the Synchrotron SED Peak

The curved 0.3–10 keV spectra mostly showed low values of the parameter b: 70% of the values from the wide range $b = 0.09$–0.64 were lower than $b = 0.3$, and only 44 spectra (5.2%) yielded $b > 0.4$. The spectra from Periods 3 to 4 exhibited the lowest curvatures with the mean values $\overline{b} = 0.23$ and 78%–85% of the spectra with $b < 0.3$ (Figures 1(Bc)–(Bd)). Note that the corresponding distributions are characterized by the significant positive skewness, i.e., by the shift of the distributions toward lower values with respect to $\overline{b}$. The majority of the spectra with narrow synchrotron SEDs (i.e., curvatures with $b > 0.4$) are mostly found in Period 2 (59%), which contains the spectrum with the highest curvature during

Table 4
Correlations between Spectral Parameters and 0.3–10 keV Flux in Different Periods

Quantities	ρ	p
	2009–2012	
a and $F_{0.3-10\ \mathrm{keV}}$	−0.81(0.04)	2.74×10^{-14}
b and a	0.21(0.07)	2.55×10^{-3}
b and E_p	−0.33(0.09)	1.34×10^{-4}
E_p and $F_{0.3-10\ \mathrm{keV}}$	0.49(0.10)	2.79×10^{-7}
$\log E_\mathrm{p}$ and $\log S_\mathrm{p}$	0.44(0.11)	3.95×10^{-6}
Γ and $F_{0.3-10\ \mathrm{keV}}$	−0.83(0.06)	1.24×10^{-14}
HR and $F_{0.3-10\ \mathrm{keV}}$	0.77(0.05)	2.09×10^{-14}
	Period 1	
a and $F_{0.3-10\ \mathrm{keV}}$	−0.77(0.04)	6.57×10^{-14}
Γ and $F_{0.3-10\ \mathrm{keV}}$	−0.67(0.05)	4.88×10^{-11}
E_p and $F_{0.3-10\ \mathrm{keV}}$	0.62(0.10)	8.46×10^{-8}
HR and $F_{0.3-10\ \mathrm{keV}}$	0.76(0.04)	3.33×10^{-13}
	Period 2	
a and $F_{0.3-10\ \mathrm{keV}}$	−0.61(0.05)	1.03×10^{-11}
E_p and $F_{0.3-10\ \mathrm{keV}}$	0.44(0.10)	4.74×10^{-6}
$\log E_\mathrm{p}$ and $\log S_\mathrm{p}$	0.49(0.10)	4.80×10^{-7}
HR and $F_{0.3-10\ \mathrm{keV}}$	0.52(0.07)	3.11×10^{-10}
	Period 3	
a and $F_{0.3-10\ \mathrm{keV}}$	−0.62(0.05)	6.12×10^{-12}
b and E_p	−0.27(0.09)	7.69×10^{-4}
E_p and $F_{0.3-10\ \mathrm{keV}}$	−0.31(0.09)	8.15×10^{-4}
$\log E_\mathrm{p}$ and $\log S_\mathrm{p}$	0.31(0.12)	8.77×10^{-4}
Γ and $F_{0.3-10\ \mathrm{keV}}$	−0.67(0.09)	5.85×10^{-9}
HR and $F_{0.3-10\ \mathrm{keV}}$	0.47(0.08)	8.89×10^{-8}
	Period 4	
a and $F_{0.3-10\ \mathrm{keV}}$	−0.78(0.03)	1.78×10^{-14}
b and E_p	−0.43(0.08)	1.08×10^{-6}
E_p and $F_{0.3-10\ \mathrm{keV}}$	−0.43(0.12)	9.15×10^{-6}
Γ and $F_{0.3-10\ \mathrm{keV}}$	−0.83(0.07)	1.35×10^{-9}
HR and $F_{0.3-10\ \mathrm{keV}}$	0.71(0.08)	5.65×10^{-12}
	Period 5	
a and $F_{0.3-10\ \mathrm{keV}}$	−0.71(0.04)	5.32×10^{-12}
HR and $F_{0.3-10\ \mathrm{keV}}$	0.69(0.05)	7.97×10^{-11}
	Period 6	
a and $F_{0.3-10\ \mathrm{keV}}$	−0.69(0.05)	4.04×10^{-11}
Γ and $F_{0.3-10\ \mathrm{keV}}$	−0.79(0.07)	5.45×10^{-10}
HR and $F_{0.3-10\ \mathrm{keV}}$	0.63(0.05)	9.13×10^{-11}

Note. For each correlation, ρ and p denote the Spearman coefficient and the corresponding p-chance, respectively.

2009–2012 (Figure 1(Bb)). In contrast, Period 3 contained only one spectrum with $b > 0.4$.

The parameter b showed a very weak positive correlation with photon index at 1 keV (see Figure 2(b) and Table 4). No correlation at the 99% confidence level was found for the samples corresponding to Periods 1–6. Figure 2(c) presents a weak anticorrelation with the position of the synchrotron SED peak (see Section 5.3 for the physical implications of these two correlations). Note that we restricted the search for the correlation b–E_p to the spectra with $E_\mathrm{p} \geqslant 0.8$ keV and $E_\mathrm{p} \leqslant 8$ keV (as explained below). This anticorrelation was found with a 99% confidence level only for Periods 5 and 6.

The position of the SED peak showed a very wide range between $E_\mathrm{p} = 0.003$ keV and $E_\mathrm{p} = 15.20$ keV. Note that 12 spectra show E_p values beyond 10 keV (5 spectra from Period 2, and 7 spectra from Period 3). However, the SED peaks of the spectra with $E_\mathrm{p} \gtrsim 8$ keV (3% of the log-parabolic spectra) are poorly constrained by the observational data, and the corresponding E_p values represent lower limits to the intrinsic peak position (see Figure 3 and Paper I). In contrast, the E_p values from the spectral analysis are systematically shifted to higher energies with respect to the intrinsic peak position when $E_\mathrm{p} \lesssim 0.8$ keV (52% of the log-parabolic spectra; see Kapanadze et al. (2016b) for the corresponding discussion). Therefore, the spectra with $E_\mathrm{p} > 8$ keV and $E_\mathrm{p} < 0.8$ keV are not used when searching for correlations of E_p with other spectral parameters. All log-parabolic spectra from Periods 5 to 6, 2012 November–December, and 91% of those from Period 1 are characterized by $E_\mathrm{p} < 0.80$ keV. In contrast, 93% of the log-parabolic spectra from Period 3 show their synchrotron SED peaks at energies higher than 0.80 keV.

Of the values with $0.8\ \mathrm{keV} \leqslant E_\mathrm{p} \leqslant 8\ \mathrm{keV}$ (i.e., the spectra with well-constrained synchrotron SEDs), 87% are included in Periods 2 an 3, and the mean values of $\overline{E_\mathrm{p}}$ are equal to 1.84 keV and 2.58 keV, respectively (see Figures 1(Cb)–(Cc) and Table 3). These periods also comprise the vast majority of the hard X-ray peaking spectra (i.e., $E_\mathrm{p} > 2$ keV; 134 out of 147). In contrast, Period 1 shows $E_\mathrm{p} < 1.07$ keV (only 11 spectra with $E_\mathrm{p} \geqslant 0.8$ keV). This parameter shows a positive correlation with the 0.3–10 keV flux, which was observed in Periods 1–4 separately (see Figure 1(d) and Table 4), although some data points from Period 3 do not follow the general trends and create outliers to the scatter plot. Finally, Figure 2(e) shows a positive correlation between $\log E_\mathrm{p}$ and $\log S_\mathrm{p}$, which was also observed in Periods 2 and 3 separately (see Table 4 and Section 5.1 for the discussion). Here, the height of the synchrotron SED peak was calculated as in Massaro et al. (2004),

$$S_\mathrm{p} = 1.6 \times 10^{-9} K 10^{(2-a)^2/4b}\ \ \mathrm{erg\ cm^{-2}\ s^{-1}}. \quad (1)$$

3.3. Power-law Spectra and Hardness Ratio

Table 5 presents the results for 61 spectra in 2009–2012, which do not exhibit a significant curvature and are well fit with a simple power law. The 0.3–10 keV photon index, derived from these spectra, also shows a very wide range of values $\Delta\Gamma = 1.18$ (see Figure 1(D)) and the hardest value $\Gamma = 1.75$ (derived from ObsID 30352218). Note that the vast majority of these spectra (95.5%) and the hardest values of the parameter Γ belong to Period 3. Only 2 power-law spectra were observed in Period 1, 5 were observed in Period 2, and 10–19 spectra were observed in other periods. Most frequently, the power-law spectra were observed in Period 6. Note that some segments of the single XRT observation yielded power-law spectra, while those from other segments showed a curvature and fit the log-parabolic model well. For example, the second, fourth, and fifth 200 s segments of ObsID 30352210 show power-law spectra with $\Gamma = 1.76$–1.79, while the spectra extracted from the first and third segments are curved with $b = 0.13$–0.14. The power-law spectra are found in diverse brightness states, and they followed a "harder-when-brighter" trend, similar to the log-parabolic spectra (see Figure 2(f) and Table 4). The data points, corresponding to highest

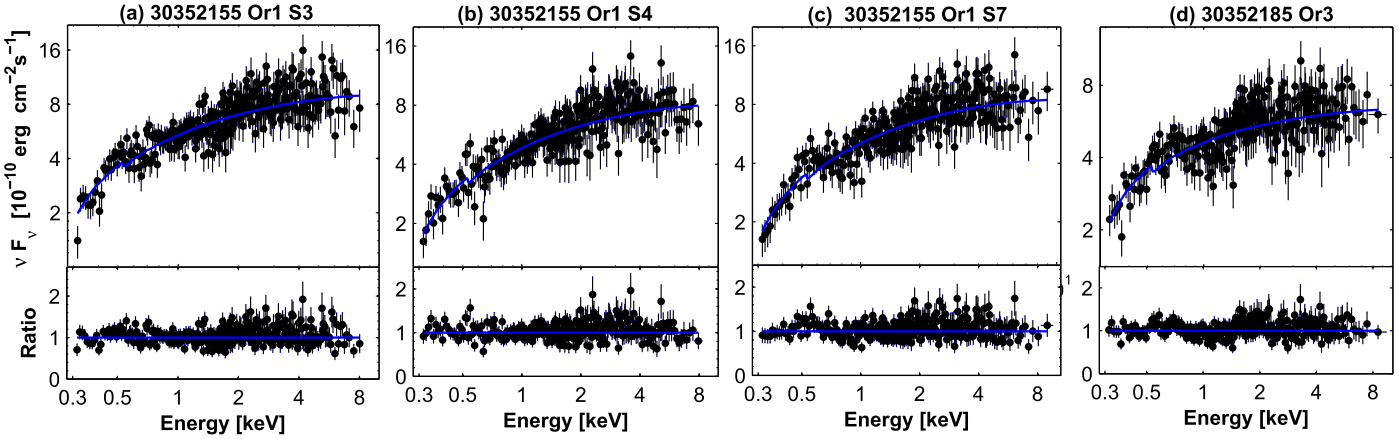

Figure 3. Examples of the 0.3–10 keV SEDs with $E_p > 10$ keV in 2009–2012 (along with the distribution of the residuals).

Table 5
Results of the XRT Spectral Analysis with a Simple Power-law Model (Extract; see the Corresponding Machine-readable Table for the Full Version)

ObsId (1)	Γ (2)	$10 \times K$ (3)	χ^2/d.o.f. (4)	$\log F_{0.3-2\,\mathrm{keV}}$ (5)	$\log F_{2-10\,\mathrm{keV}}$ (6)	$\log F_{0.3-10\,\mathrm{keV}}$ (7)	HR (8)
30352124 Or2	2.22(0.04)	2.49(0.06)	0.89/55	−9.09(0.01)	−9.33(0.02)	−8.89(0.01)	0.58(0.04)
30352139	2.39(0.03)	1.90(0.04)	1.00/74	−9.19(0.01)	−9.56(0.02)	−9.03(0.01)	0.49(0.02)
31540003	1.92(0.03)	2.49(0.05)	1.08/75	−9.13(0.01)	−9.14(0.02)	−8.84(0.01)	0.97(0.05)
30352185 S1 (210 s)	1.87(0.01)	2.93(0.03)	1.06/265	−9.06(0.01)	−9.04(0.01)	−8.75(0.01)	1.06(0.02)

Note. In Column 1, the abbreviations "Or" and "S" stand for "Orbit" and "Segment," respectively. Unabsorbed 0.3–2 keV, 2–10 keV, and 0.3–10 keV fluxes (Columns 5–7) are given in erg cm^{-2} s^{-1}.

(This table is available in its entirety in machine-readable form.)

brightness states, do not follow the general trend (similar to the log-parabolic spectra observed in the highest states).

The values of the hardness ratio, derived from log-parabolic and power-law spectra, showed that a wide range ΔHR = 1.37. 56% of the values are higher than HR = 0.5, and 106 spectra (11%) show HR $\geqslant$ 1 (see Table 3). The latter belong to Periods 1–4, while all values from Period 5 and 2012 November–December are lower than 0.5 (see Figure 1(E)). Note that the lowest historical value HR = 0.11 belongs to Period 5 (the aforementioned spectrum with the highest value of parameter *a*). A vast majority (95%) of the spectra from Period 6 also show HR < 0.5. These results are reflected in the large difference of the mean values in different periods, which range from $\overline{\mathrm{HR}} = 0.26$ (Period 5) to $\overline{\mathrm{HR}} = 0.88$ (Period 3). A positive correlation between HR and the unabsorbed 0.3–10 keV flux is observed in all periods (Figure 2(g)), confirming the dominance of a "harder-when-brighter" spectral evolution during X-ray flares. Note that this trend was strongest in Period 2, while it was significantly weaker in Periods 2 and 4 (see Table 4). Some sub-samples from these periods produce outliers from the scatter plot. Nevertheless, one sub-sample from Period 3 (the data points corresponding to the spectra extracted from the segments of ObsID 31630001) follow a "softer-when-brighter" trend (the right lower outlier in Figure 2(g)).

4. Flux and Spectral Variability

4.1. Long-term X-Ray and MWL Variability

During 2009–2012, the source was very strongly variable in X-rays: the 0.3–10 keV count rate showed a range between 1.89 cts s^{-1} (the lowest historical value, observed on 2011 February 14, MJD 55606.2) and 114.73 cts s^{-1} (2010 February 17, MJD 55244.0) with a weighted mean value of 18.33 cts s^{-1}. It showed a number of X-ray flares with various amplitudes, observed within time intervals ranging from several days to about two months (see below). Although the mean 0.3–10 keV rate in 2009–2012 was lower than in 2005–2008 (Kapanadze et al. 2018), 2013 January–May (Kapanadze et al. 2016a), and 2013 November–2015 June (Kapanadze et al. 2017a), Mrk 421 was brightest and one of the most violently variable blazars in X-rays during the period presented here.

Below, we concentrate on the results in Periods 1–6, whose summary from the XRT and UVOT observations is presented in Table 6: maximum 0.3–10 keV count rates, unabsorbed 0.3–10 keV, 2–10 keV, and UVOT-band fluxes, maximum-to-minimum flux ratios, and fractional variability amplitudes in each band calculated as $F_{\mathrm{var}} = 100\,((S^2 - \overline{\sigma^2_{\mathrm{err}}})/\overline{F})^{1/2}$ %, with S^2 the sample variance, $\overline{\sigma^2_{\mathrm{err}}}$ the mean square error, and $\overline{F}$ the mean flux (Vaughan et al. 2003). The MWL light curves from each period are presented in Figure 4.

In Period 1,[8] the source underwent two subsequent 0.3–10 keV flares by a factor of ~3 on weekly timescales (Figure 4(a)), accompanied by enhanced VHE activity (flares by a factor of 3–5).[9] The LAT-band flux did not show clear

[8] See Table 6 for the periods mentioned in this subsection.

[9] The VHE light curves were constructed using the VERITAS data from http://veritas.sao.arizona.edu/veritas-science/veritas-blazar-spectra, Alecsic et al. (2015a, 2015b; Balocovic et al. 2016), as well as those obtained with MAGIC (Steinke 2012; Preziuso 2013; Alecsic et al. 2015a, 2015b; Ahnen et al. 2016), Whipple (available at http://veritas.sao.arizona.edu/veritas-science/mrk-421-long-term-lightcurve), and HAGAR (Sinha et al. 2016). The VHE fluxes, provided in units of ph cm^{-2} s^{-1}, were converted into Crab units using the recipes provided in Paper I.

Table 6
Summary of the XRT and UVOT Observations of Mrk 421 in Different Periods (Defined in Columns 1–2)

		XRT								UVOT						
Per. (1)	Dates (2)	$CR_{\max}$ (3)	R (4)	$F_{\rm var}$ (5)	$F^{\max}_{2-10}$ (6)	R_{2-10} (7)	$F_{\rm var}$ (8)	$F^{\max}_{0.3-2}$ (9)	$R_{0.3-2}$ (10)	$F_{\rm var}$ (11)	$R_{\rm W2}$ (12)	$F_{\rm var}$ (13)	$R_{\rm M2}$ (14)	$F_{\rm var}$ (15)	$R_{\rm W1}$ (16)	$F_{\rm var}$ (17)
1	54843.8–54978.9	46.31	3.0	44.8(0.1)	5.57	7.9	26.5(0.1)	8.51	3.8	23.1(0.1)	2.2	23.7(0.4)	3.0	27.7(0.3)	2.0	18.6(0.6)
2	55147.7–55227.2	93.66	26.4	41.9(0.1)	20.32	85.4	50.8(0.1)	17.46	20.3	29.4(0.1)	2.0	18.8(0.4)	2.2	19.5(0.5)	1.8	14.9(0.6)
3	55228.3–55299.1	114.73	12.8	53.8(0.1)	26.67	48.4	43.4(0.1)	22.34	12.3	35.5(0.1)	2.2	20.4(0.3)	2.0	18.2(0.2)	2.1	20.9(0.5)
4	55303.1–55391.1	49.80	10.5	62.6(0.1)	14.17	57.6	55.3(0.1)	14.39	14.9	39.8(0.1)	1.6	14.2(0.4)	1.8	15.9(0.3)	1.8	14.0(0.6)
5	55533.5–55722.1	26.32	13.9	50.8(0.2)	2.04	38.5	69.2(0.2)	5.41	12.0	48.2(0.1)	3.2	26.8(0.3)	3.5	26.0(0.2)	3.3	25.4(0.4)
6	55839.9–56078.5	43.41	11.5	51.7(0.2)	4.13	39.0	76.8(0.2)	8.51	11.4	51.6(0.1)	2.3	18.2(0.3)	2.7	22.6(0.2)	2.4	19.7(0.4)

Note. Columns 3–5: maximum 0.3–10 keV flux (in cts s^{-1}), maximum-to-minimum flux ratio, and fractional amplitude (in percent), respectively; maximum unabsorbed flux (in 10^{-10} erg cm^{-2} s^{-1}), maximum-to-minimum flux ratio and fractional amplitude in 2–10 keV (Columns 6–8), 0.3–2 keV (Columns 9–11) bands; and maximum-to-minimum flux ratio and fractional amplitude in UVW2 (Columns 12–13), UVM2 (Columns 14–15) and UVW1 (Columns 16–17) bands.

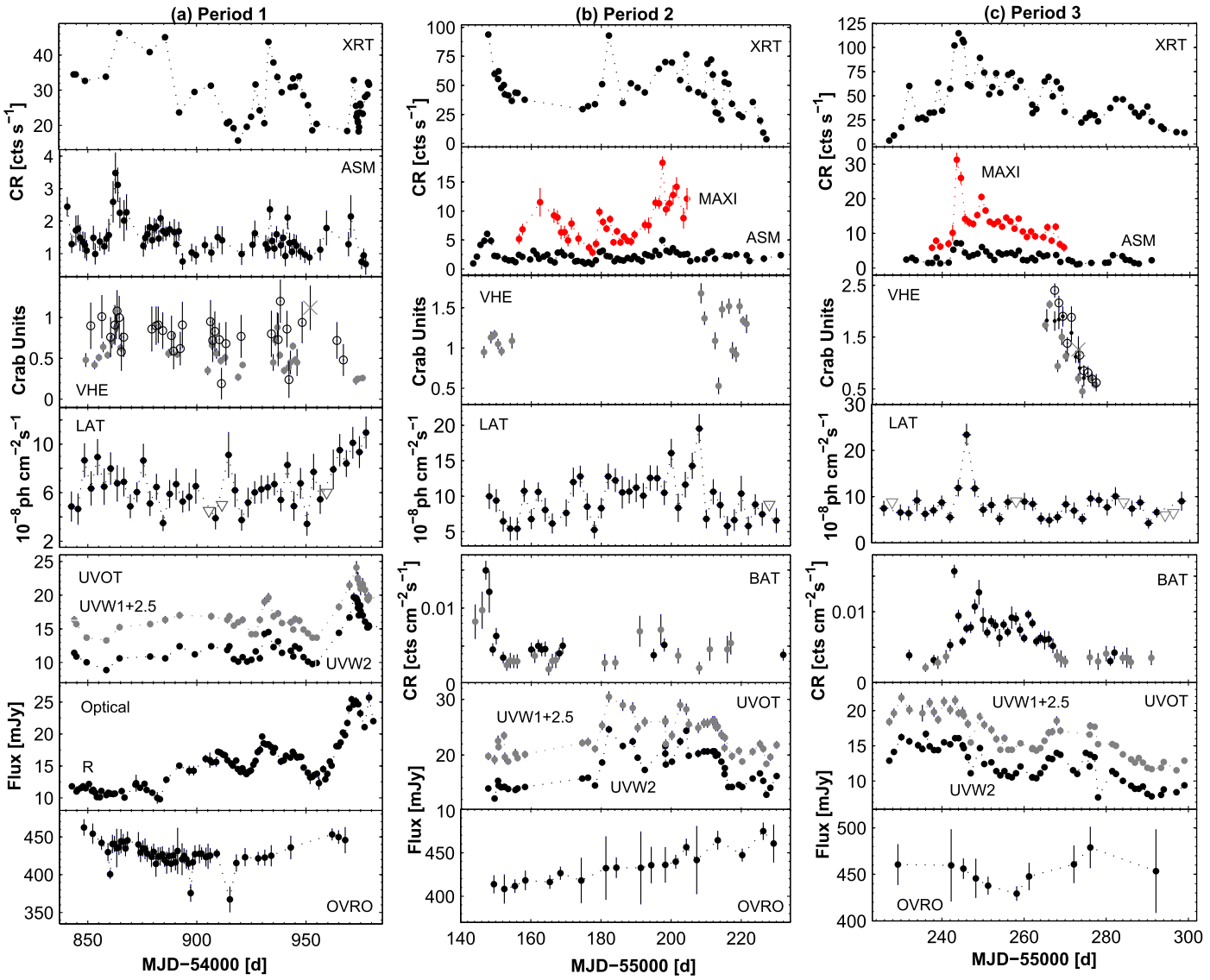

Figure 4. MWL variability of Mrk 421 in different periods during 2009–2012. The daily bins are used for the XRT, FACT, UVOT, Steward, 15 GHz, and light curves and the two-day bins for the LAT data. The radio-band observations were performed with the 40 m OVRO telescope (Richards et al. 2011), and the corresponding data are retrieved from http://www.astro.caltech.edu/ovroblazars/). In the VHE light curves, black points correspond to the VERITAS data, and the gray points, circles, and asterisks correspond to those from the MAGIC, Whipple, and HAGAR observations, respectively. The triangles in the LAT-related plots stand for the 2σ upper limits to the 0.3–300 GeV flux when the source was detected below the 3σ significance. The BAT detections of Mrk 421 with 5σ and 3σ significances are shown with with black and gray points, respectively (see the next page for Figures 4(d)–(f)).

flares along with the X-ray ones, and a highest 0.3–300 GeV state was observed around MJD 54915 when the source showed its low X-ray state. However, another enhanced HE activity was observed at the end of this period when the source exhibited two fast, lower-amplitude flares by ∼80%. During these days, UV and optical[10] fluxes doubled and reached their highest values. The previous, lower-amplitude peak was observed in the epoch of the second X-ray flare (during MJD 54919–54953). However, the source was in its low UV–optical state during the first X-ray flare.

During most of Period 2, the source showed a higher X-ray state, superimposed by two fast flares by factors of 2.6 and 2.9 around MJD 55148 and MJD 55182, respectively, when the 0.3–10 keV count rate reached almost a level of 100 cts s^{-1} (Figure 4(b)). During MJD 55157–173, the MAXI observations[11] in the 2–20 keV energy range revealed a flux doubling (not covered by XRT observations). Another strong flare by a factor of ∼3 was detected with this instrument during MJD 55188–55203, while we observe a brightness enhancement only by 75% in the XRT band (probably due to stronger flaring activity of the source at energies higher than 10 keV). The next two minor 0.3–10 keV flares were accompanied by two fast VHE flares by a factor ∼3, as well as by an HE flare by

[10] The optical magnitudes in the *V* and *R* bands are extracted from the website http://james.as.arizona.edu/~psmith/Fermi/, which presents the results obtained with the 2.3 and 1.5 m telescopes of the Steward Observatory (Smith et al. 2009); see Paper I for the recipes used to perform corrections on the Galactic absorption and host contribution.

[11] Retrieved from http://maxi.riken.jp/. We used only the detections with 5σ significance for our purposes. Along with the MAXI light curves, we plotted those constructed using the 1.5–12 keV data obtained with All-Sky Monitor (ASM) on board the *Rossi X-ray Timing Explorer* (*RXTE*, Levine et al. 1996), which are available at http://xte.mit.edu/asmlc/ASM.html.

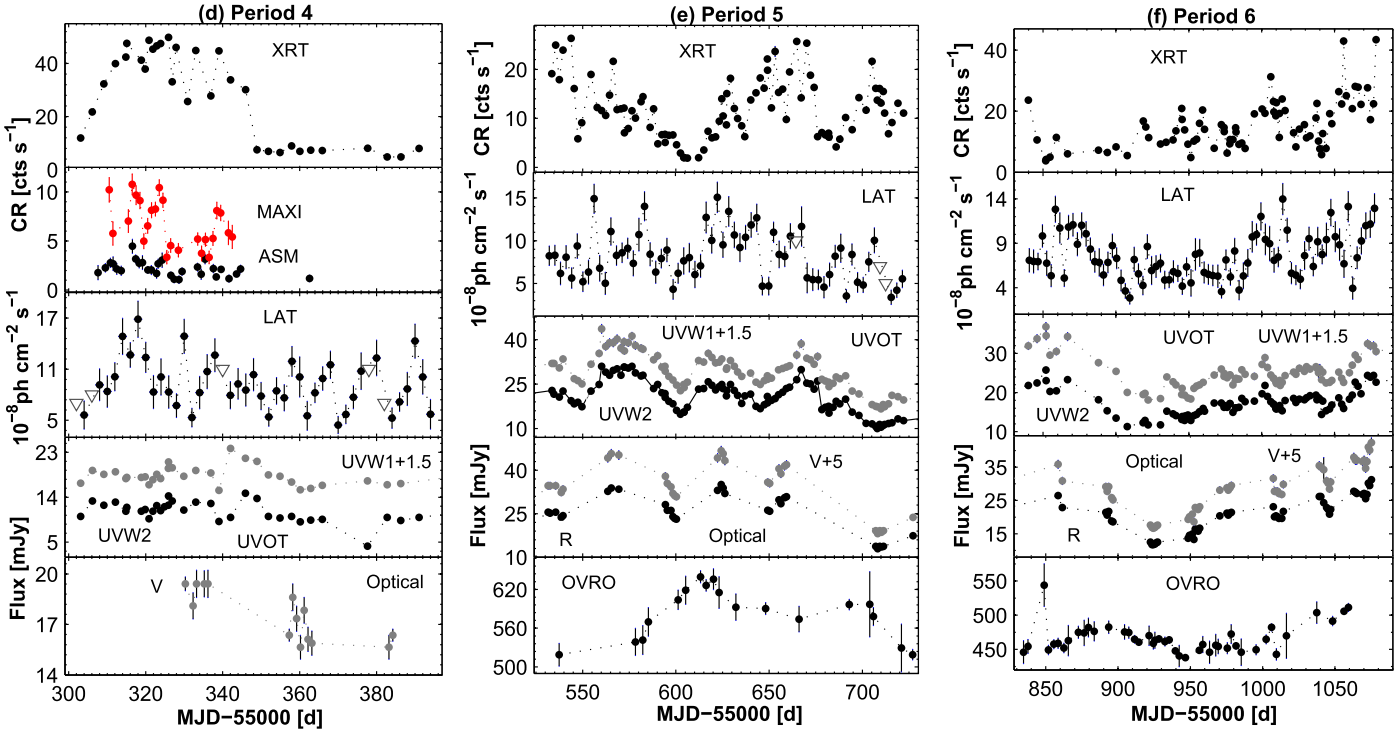

Figure 4. (Continued.)

a factor of 2.3. A BAT-band flare[12] by a factor of ∼6 and high VHE states (∼1 Crab) were observed also in the beginning of this period, along with the 0.3–10 keV flare. The second XRT-band flare and subsequent minor ones were accompanied by enhanced UV states.

In the beginning of Period 3, the source showed an unprecedently low 0.3–10 keV brightness (corresponding to 3.55 cts s^{-1}), followed by a permanent brightness increase by a factor of ∼17 during the next 20 days (Figure 4(c)). This brightening was accompanied by fast flares by a factor of 3.3–3.5, and the 0.3–10 keV rate reached its highest value during 2009–2012 on MJD 55244 (corresponding to a 32-fold increase in brightness). Afterward, the source showed a long-term decline by a factor of 6.4 during 1.5 months, accompanied by minor brightness fluctuations. A similar behavior was observed in the BAT-band. The VHE data are available only for the period MJD 55265–55277, and they show a brightness drop by a factor of 4.2 from the level of 2.4 Crab, corresponding to the highest VHE state observed during 2009–2012 (along with minor 0.3–10 keV flare during the long-term decline). The LAT observations showed a fast HE flare by a factor of 5.5 in the epoch of the highest 0.3–10 keV states and did not vary significantly in other parts of this period. As for the UV fluxes, they showed a long-term declining trend during almost the whole period (with some low-amplitude variations), not showing a correlation with those from the higher-energy bands.

The source underwent a strong prolonged flare by a factor of 4 (lasting about 1.5 months) in the first half of Period 4, and it showed a low 0.3–10 keV state during the subsequent 1.5 month interval without significant flux variability. The latter behavior is uncommon for this violently variable HBL source (Figure 4(d)). The LAT-band observations recorded HE flares by a factor of 2.3–3.0 in the epoch of X-ray flare, although it showed a similar behavior also in the second half of this period.

During Periods 5–6 (separated by an about four-month interval from each other), Mrk 421 generally showed one of the lowest 0.3–10 keV states during the 12 year of *Swift* observations (Figures 4(e)–(f)). Although it underwent several flares by a factor of 3.7–9.5 in these periods, the highest count rates at flare peaks were mostly below 30 cts s^{-1}, while the mean count rate during 2005–2015 was about 33 cts s^{-1}. In contrast, the HE flux was not lower than that observed in the previous periods and showed a moderate flaring behavior with a few correlations with that observed in the XRT band. On average, the UV and optical fluxes were significantly higher than in previous years, and the corresponding light curves did not exhibit any correlation with the 0.3–10 keV one.

4.2. Spectral Variability

Figure 5(b) shows that the photon index at 1 keV varied on diverse timescales during 2005 March–2008 June. The largest hardenings were observed during MJD 55226–55232 (a = 2.54–1.90) and MJD 54303–55315 (a = 2.43–1.86). As for the opposite trend, large softenings with Δa = 0.82–0.93 were recorded during MJD 55147.8–55149.5, 55204.3–55205.6, and 55215.3–55226.3. This parameter often varied by Δa = 0.09–0.49 on intraday timescales with 3σ significance, generally

[12] From the daily binned BAT data, obtained within the *Swift*-BAT Hard X-ray Transient Monitor program (Krimm et al. 2013) and provided at http://swift.gsfc.nasa.gov/results/transients/weak/Mrk421/, we used only those corresponding to the detection of the source with 5σ significance (the threshold generally accepted for coded-mask devices) to study a variability of the 15–150 keV flux. However, we also plotted the data corresponding to their detection with 3σ significance in Figure 4 (used by some authors for flux variability study; see, e.g., Horan et al. 2009).

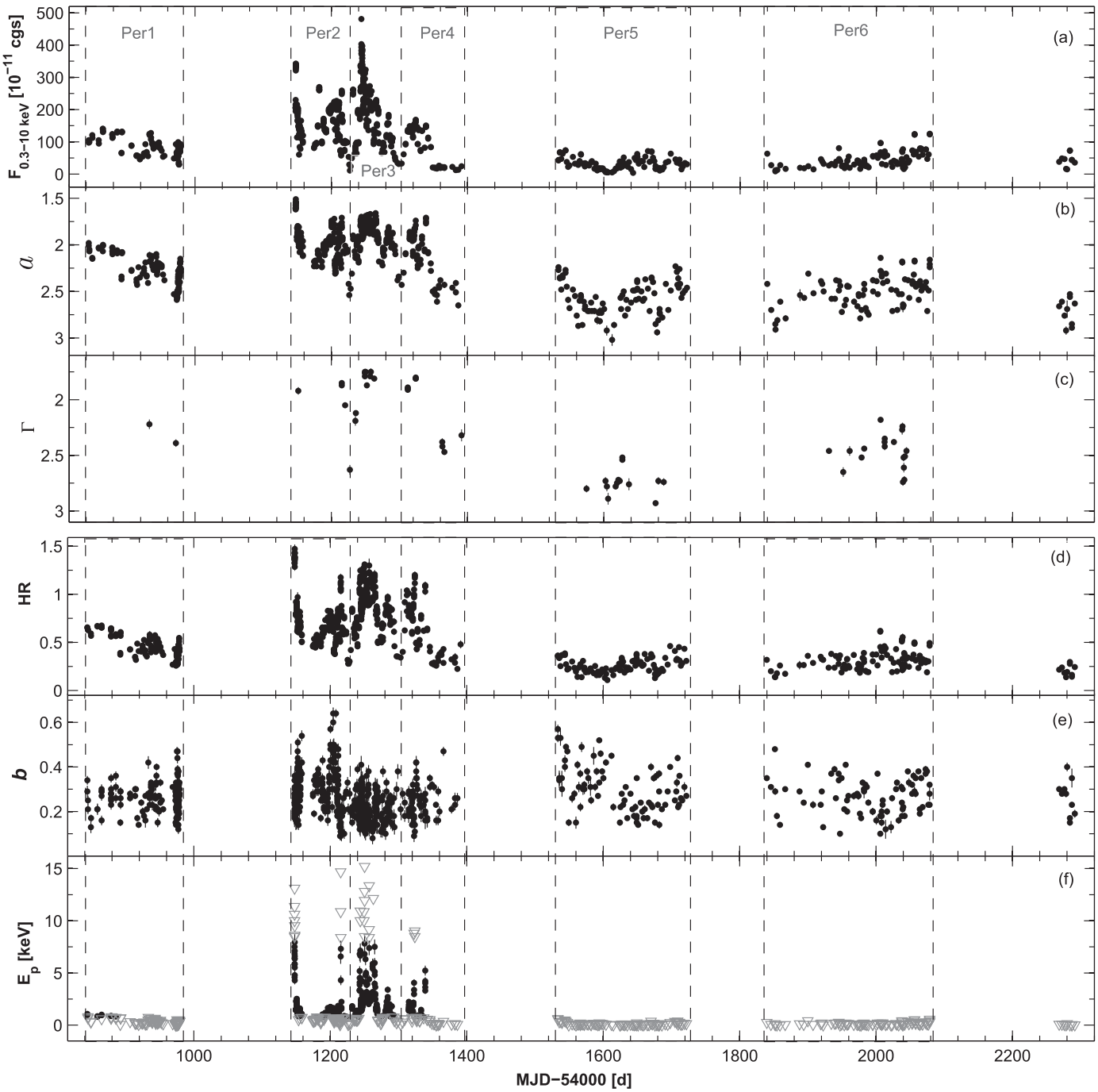

Figure 5. Unabsorbed 0.3–10 keV flux (top panel), photon index (panel (b)), hardness ratio (panel (c)), curvature parameter (panel (d)), and E_p (bottom panel, with the triangles denoting upper or lower limits) plotted vs. time.

associated with the intraday-variability (IDV) events (see Section 4.4 and Table 7 for details). However, this variability was not observed on sub-hour timescales with this significance, in contrast to the periods 2005–2008 and 2013 January–May, when the photon index varied even within 1 ks observational runs.

Similar to the parameter a, the 0.3–10 keV photon index varied on diverse timescales, and it showed a large softening by $\Delta\Gamma = 0.76$ during MJD 55215.3–55227.2, followed by a hardening by $\Delta\Gamma = 0.88$ during the next 22-day interval (Figure 5(c)). On intraday timescales, the source underwent a softening by $\Delta\Gamma = 0.50$ within 12 hr (on MJD 56038).

The hardness ratio also often varied on intraday timescales during the 0.3–10 keV IDVs (see Table 7) and showed increases by a factor of 2.06–2.32 within 17–21 hr (during MJD 55214.41–55215.27 MJD 56037.29–56037.98; (Figure 5(d))). On longer timescales, this parameter showed large increases by a factor of 2.18–3.84 and dropped by a factor of 1.90–2.92, associated with the aforementioned large variabilities of the photon indices.

The curvature parameter varied 26 times with 3σ significance by $\Delta b = 0.17$–0.36 (see Table 7) with the fastest event incorporating an increase by $\Delta b = 0.17$ during 0.5 hr (the first orbit of ObsID 31630001). On longer timescales, the parameter

Table 7
Summary of the 0.3–10 keV IDVs in 2008 March–2008 June (Extract; See the Corresponding Machine-readable Table for the Full Version)

ObsID(s) (1)	Dates (2)	ΔT(hr) (3)	χ^2/dof (4)	Bin (5)	F_{var}(%) (6)	a or Γ (7)	b (8)	E_p (keV) (9)	HR (10)
30352108	2009 Feb 02	3.15	29.42/2	Or	3.9(0.4)	2.00(0.02)−2.07(0.02)	0.16(0.04)−0.30(0.05)	0.60(0.06)−1.00(0.09)	0.65(0.02)−0.68(0.02)
30352109	2009 Feb 14	2.65	49.04/1	Or	3.5(0.4)	2.03(0.03)−2.10(0.02)	0.23(0.04)−0.35(.04)	0.70(0.07)−0.88(0.08)	0.56(0.02)−0.64(0.03)
30352127	2009 Apr 17	3.65	29.42/2	Or	4.5(0.6)	2.22(0.02)−2.27(0.02)	0.23(0.05)−0.23(0.07)	0.27(0.04)−0.43(0.05)	0.43(0.01)−0.45(0.02)
(303521)30-31	2009 Apr 23	21.75	39.45/3	Or	3.9(0.4)	2.19(0.02)−2.32(0.02)	0.21(0.04)−0.40(0.05)	0.17(0.03)−0.49(0.05)	0.40(0.01)−0.50(0.02)

Note. In Column 1, "Or" stands for "Orbit." The third column gives the total length of the particular observation (including the intervals between the orbits). Columns 7–10 give the ranges of the photon index, curvature parameter, the position of the synchrotron SED peak, and the hardness ratio. In Column 7, the acronyms "LP" and "PL" denote log-parabolic and power-law spectra, respectively.

(This table is available in its entirety in machine-readable form.)

b showed the largest decrease from its highest value by $\Delta b = 0.55$ in seven days (Figure 5(e)).

In the case of well-constrained synchrotron SED peaks, the parameter E_p showed largest shifts by 5.4–6.1 keV in 0.7–2.8 days toward higher frequencies, and the opposite trend by 4.9–6.5 keV in 1.0–4.0 days was also observed (Figure 5(f)). Indeed, some out of these shifts are larger and could exceed ΔE_p10 keV, taking into account upper limits to this parameter. On intraday timescales, this parameter varied 31 times, with amplitudes ranging from $\Delta E_p = 0.55$ to $\Delta E_p > 7.20$ keV (taking into account upper limits).

4.3. Intraday Flux and Spectral Variability

During 2009–2012, the source was often active on very short timescales. We detected 118 instances of intraday 0.3–10 keV IDV, defined as a flux change with 99.9% confidence within a day (the threshold generally used for this purpose; see, e.g., Andruchow et al. 2005) using the χ^2-statistics. Table 7 presents the values of reduced χ^2, fractional variability amplitude, and the ranges of the spectral parameters for each IDV.

4.3.1. The Fastest IDVs

The source underwent very fast variability during the 2010 February 18 (MJD 55245) observation when it showed one of the highest X-ray states (Figures 6(a)–(b)). During the first orbit of this observation, the source twice showed a decline by about 10% within 180–720 s and fluctuated by 8%–11% within 240–420 s during the second orbit, separated by 4.8 ks interval from the first one. In the case of another very high X-ray state, observed on 2009 November 12 (MJD 55147), the flux exhibited a decline by 22% within 240 s (Figure 6(c)). The source also underwent a very fast decline by 9% during 480 s when it showed the highest daily binned count rate (Figure 6(d)).

Mrk 421 showed a flux variability within 1 ks observational runs also in lower X-ray states. Namely, it underwent brightness declines by 8%–22% within 180–900 s (Figures 6(e), (g), (h), (i), (k), and (n)), and brightenings by 7%–24% within 180–720 s (Figures 6(f), (h), (i), (j), (l), and (n)). During these events, the parameters a and b showed a variability only at the 1σ–2σ confidence level.

In the case of well-constrained synchrotron SED peaks, their positions shifted by 0.4–1.9 keV within 470–570 s (Figures 6(a), (c), and (f)) toward higher frequencies and showed an opposite trend by 3.31–6.20 keV within 280–840 s (Figures 6(d) and (f)). In fact, this parameter varied with larger amplitudes during the IDVs presented in Figures 6(c)–(d). However, we cannot draw a firm conclusion about the value of ΔE_p because of the peak beyond 8 keV.

4.3.2. IDVs from the Extended XRT Observations

Figure 7(a) presents the light curves of the most densely sampled XRT observations of Mrk 421 performed during 2009 May 22–27, which lasted up to 515 ks (including the intervals between consecutive orbits). During this campaign, the most extreme variability included brightness drops by a factor of 2.1–2.2 in 5.7–6 ks (during $t = 243.1$–248.8 ks and $t = 323.8$–329.8 ks since the start of the campaign) and increases by a factor of 2.25–2.45 in 27.3–57.6 ks (during $t = 295.1$–323.8 ks and $t = 329.8$–387.5 ks). Using the equation $\tau_{d,h} = \Delta t \times ln(2)/ln(F_2/F_1)$ (Saito et al. 2013), we obtain flux-doubling and halving times $\tau_d = 6.5$–12.4 hr and $\tau_h = 1.4$–1.5 hr, respectively. However, other parts of the light curve present significantly slower variability (changes by only 28%–62% in 18–173 ks). The spectra hardened by $\Delta a = 0.09$–0.44 in 23.1–75.5 ks and softened by $\Delta a = 0.15$–0.24 in 23.1–40.5 ks, mainly showing a "harder-when-brighter" spectral evolution. However, the source did not exhibit a clear trend during $t = 0.0$–81.5 ks, 254.6–283.5 ks, and 433.8–514.9 ks and followed an opposite one during $t = 283.5$–295.0 ks and 410.7–433.8 ks. The parameter b varied by $\Delta b = 0.19$–0.33 within 11.6–46.6 ks, and the synchrotron SED peak was always situated at energies below 0.8 keV.

The source underwent a 2.2-fold decrease of the brightness in about 85.5 ks during 2010 February 18–19 (accompanied by a spectral hardening by $\Delta a = 0.15$) and did not show strong variability afterward, although the parameter ΔE_p shifted by 2.70 keV toward higher frequencies (in 51.9 ks) and then moved back by 2.45 keV (in 44.3 ks) in that case (Figure 7(b)).

The source showed very interesting behavior during 2009 February 15–17 (Figure 7(c)): the 0.3–10 keV flux dropped by a factor 2.2 in 4 ks (associated with a softening by $\Delta a = 0.21$), followed by an 2.1-fold increase during the next 1.7 ks. The X-ray brightness dropped by a factor 3 in 116 ks during 2010 January 15–16 (Figure 7(d)) and showed two halving instances in turn (each in 76.5–80.2 ks) during 2010 January 30–31 (Figure 7(g)). Finally, flux-doubling instances were observed during 2010 February 11–12 (in 85.7 ks; Figure 7(e)) and during 2012 March 23–24 (in 38.9 ks; Figure 7(f)).

5. Discussion and Conclusions

5.1. Flux Variability

5.1.1. Variability Amplitudes

In this paper, we have presented the results of a detailed spectral study of the nearby TeV-detected blazar Mrk 421 based on the rich archival data obtained with *Swift*–XRT during 2009 January–2012 December. During the four-year period we presented here, Mrk 421 showed strong X-ray flaring activity by a factor of 3–17 on timescales of a few days–weeks and a maximum-to-minimum flux ratio of 58.5 in the XRT band. The 0.3–10 keV count rate exceeded the threshold of 100 cts s^{-1} for the second time from the start of *Swift* observations during 2010 February 16–18, and attained a value of 114.7 cts s^{-1} (a daily binned value, corresponding to the deabsorbed flux of 4.1×10^{-9} erg cm^{-2} s^{-1}), and it was 33% lower than that observed on 2008 June 12. In the case of 2-minute bins, the highest count rate was 122.34 ± 1.48 cts s^{-1} (corresponding to 4.8×10^{-9} erg cm^{-2} s^{-1}). This value was recorded in the course of the flare starting from one of the lowest historical 0.3–10 keV level, and the maximum-to-minimum flux ratio during this event $R = 32.3$. Note that this quantity was significantly smaller during the giant X-ray flare in 2013 April, when the 2-minute binned 0.3–10 keV rate exceeded the level of 260 cts s^{-1} ($R \approx 22$) and it was impossible to calculate this quantity in 2008 June since the aforementioned very high state was not preceded by XRT observations. Table 8 demonstrates that Mrk 421 was generally the brightest HBL source in the X-ray sky during 2009–2012, similar to other periods.

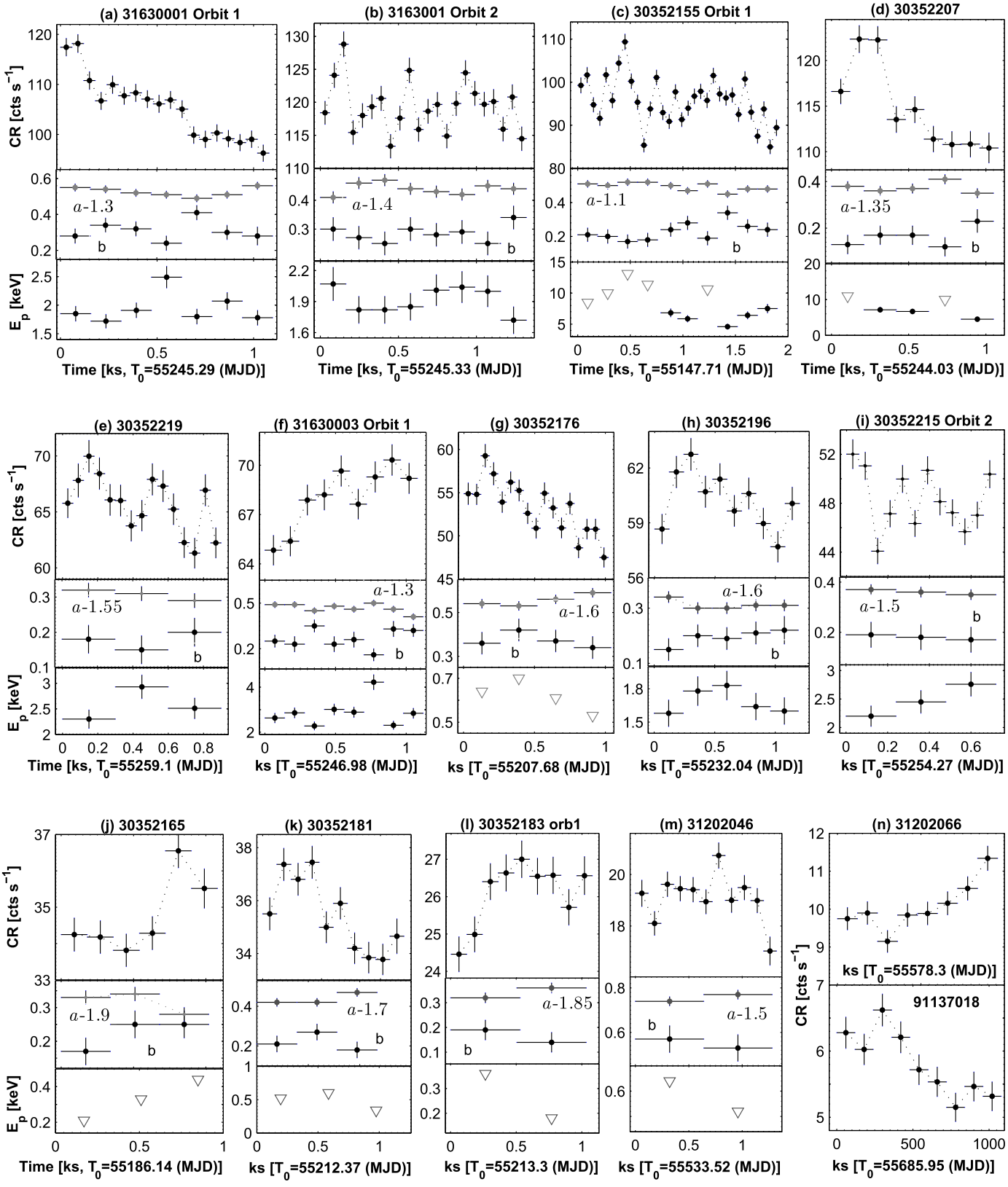

Figure 6. Fastest 0.3–10 keV IDVs in 2009–2012.

However, the source was in a quiescent state during about 1.5 months in 2010 June–July, which is uncommon for this violently variable blazar. This feature could be related to absence of a strong shock wave, triggered by the abrupt increase of the collimated matter in the jet base and propagating downstream the jet with a relativistic velocity that can cause a long-term flare in different spectral bands (the so-called shock-in-jet scenario; Sokolov et al. 2004).

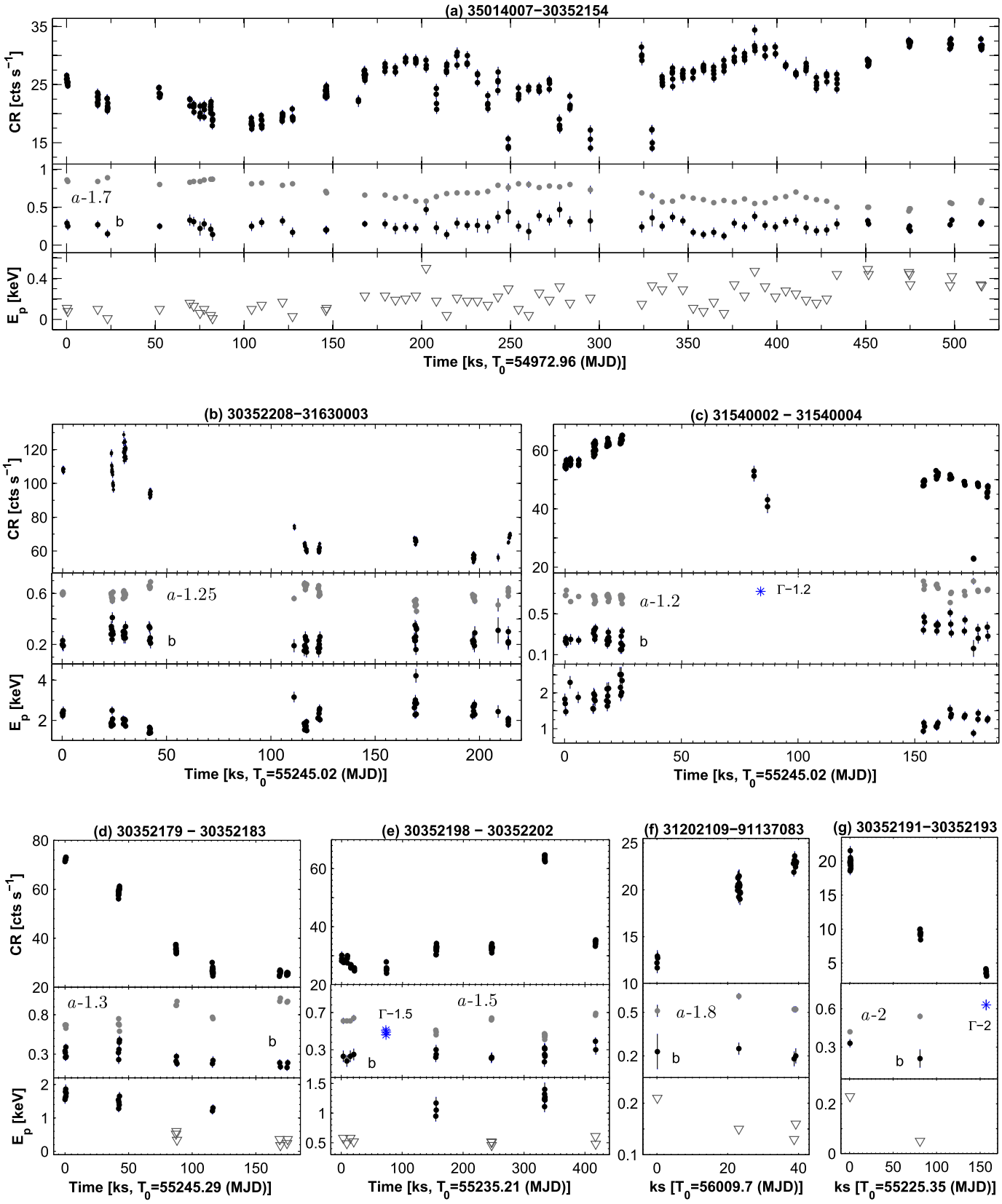

Figure 7. Most densely sampled 0.3–10 keV light curves with brightness doubling/halving in 2009–2012.

Note that the source was detected only 24 times with 5σ significance in the 15–150 keV energy range from the daily binned BAT data, in contrast to 75 detections within 2005 March–2008 June, and this result is related to the presence of the synchrotron SED peak position beyond 10 keV, which occurred more frequently in the latter period. Note also that Mrk 421 did not show as strong 15–150 keV flares during 2009–2012 as in previous years, and it was detected with the

Table 8
Ranges of Unabsorbed 0.3–2 keV and 2–10 keV Fluxes (in Units of 10^{-11} erg cm^{-2} s^{-1}) of Bright HBLs in Different Periods

Per.	$F^{\rm min}_{0.3-2{\rm keV}}$	$F^{\rm max}_{0.3-2{\rm keV}}$	$F^{\rm min}_{2-10{\rm keV}}$	$F^{\rm max}_{2-10{\rm keV}}$	References
		Mrk 421			
1997 April–2002 December	...	...	4.10	93.20	M04, R04
2005 March–2008 June	15.17	261.82	3.50	312.35	K18a
2009 January–2012 December	4.52	223.36	0.53	266.69	TW
2013 January–May	10.74	313.33	2.88	392.64	K16a
2013 November–2015 June	19.72	166.72	4.37	140.93	K17a
		1ES 1959+650			
1997 May–2002 November	...	...	0.84	29.30	G02, P05, M08
2005 April–2014 September	4.22	30.50	1.91	24.3	K16c
2015 August–2016 August	11.17	34.67	6.17	50.58	K16b
		Mrk 501			
1997 April 7–2007 April	...	...	3.02	52.40	M08
2014 March–October	7.21	33.19	6.04	53.20	K17b
		PKS 2155-304			
1996 November–2006 May	...	...	1.22	8.23	M08
2005 November–2012 October	1.69	25.68	0.36	11.37	K14

Note. The references in the last column are as follows: R04, Ravasio et al. (2004); TW, this work; K18a, Kapanadze et al. (2018); K17a, Kapanadze et al. (2017a); K16b, Kapanadze et al. (2016b); G02, Giebels et al. (2002); P05, Perlman et al. (2005); K16c, Kapanadze et al. (2016c); and K14, Kapanadze et al. (2014).

aforementioned significance during the significant part of this period (2011 September–2012 December).

Unfortunately, the source was not observed with XRT during 2012 June–October when the source underwent its strongest long-term 0.3–300 GeV flare during the 2008–2016 period (see Kapanadze et al. 2017a). Contemporaneous *MAXI* observations revealed only a modest X-ray flaring activity, and the source was not detectable with 5σ significance[13] from the weekly binned data. We have checked that these MAXI-detected flares are evident only in the 2–10 keV energy range, while it was mostly not detectable and did not show enhanced X-ray activity at higher energies. This result is in agreement with the fact that BAT did not detected Mk 421 with 5σ significance in the epoch of the LAT-band flare, and it can be related to the possibility that the X-ray emitting electrons were not accelerated to the energies that are necessary for the emission of the photons at energies $E > 10$ keV by means of the synchrotron mechanism. During the aforementioned flare, the source was generally detectable with 3σ significance from the daily binned LAT data, while we had to use the 2–3-day bins to construct the 0.3–300 GeV light curves in Periods 1–6, which were characterized by moderate HE flaring activity (see Figure 4).

In the epoch of the aforementioned LAT-band event, the source also underwent its strongest 15 GHz flare since the start of the OVRO operations, with a peak showing a delay by ~30 day with respect to the 0.3–300 GeV one, and the radio flux exceeded a threshold of 1 Jy, which is uncommon for HBLs at radio frequencies (Howatta et al. 2015). Assuming a physical connection between the γ-ray and radio flares, Howatta et al. explained the observed sharp radio flare using a one-zone SSC model, although the model parameters required a fine tuning. The same authors proposed another explanation involving an SSC model plus time variations of the Doppler factor.

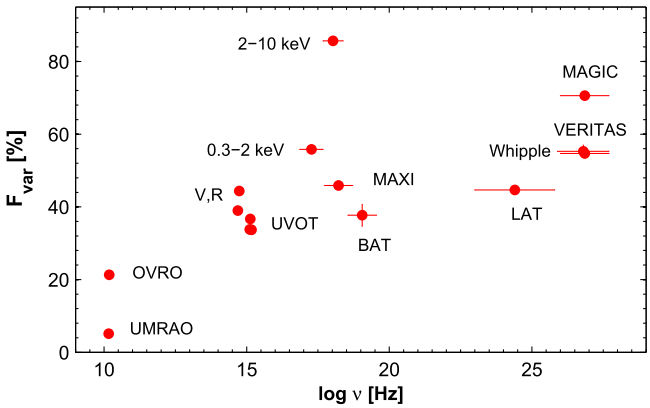

Figure 8. $F_{\rm var}$ quantity as a function of the energy in different periods.

In the $F_{\rm var}$–logν plane, where the $F_{\rm var}$ values from each band are calculated using all the available data obtained with various instruments[14] during 2009–2012, Mrk 421 showed a double-peaked shape with the highest variability in the X-ray and VHE bands (Figure 8). A similar shape observed also in the periods 2005–2008, 2013 April, 2013 November–2014 May, and 2015 January–June (see Kapanadze et al. 2016a, 2017a, 2018). Note that the value of $F_{\rm var}$ is known to be dependent on the data sampling, and this result should be interpreted with caution. Generally, $F_{\rm var}$ was derived using the individual single-day measurements of our target, except for the fractional amplitude in the 0.3–300 GeV energy range from the LAT observations, for which, because of the limited sensitivity, we used data integrated over 2 days–1 week in different periods.

[13] The threshold generally adopted for the flux variability studies with this instrument (T. Mihara 2018, private communication).

[14] The 14.5 GHz observations were performed with the 26 m telescope of the University of Michigan Radio Astronomy Observatory (UMRAO; Aller et al. 1985).

For the calculation of fractional variability amplitude from the ASM, BAT, Whipple, VERITAS, MAGIC, and the First G-APD Cherenkov Telescope (FACT) observations, we used only the flux values from those time bins when the source was detected with 3σ–5σ significances.

In the synchrotron part of the spectrum, Figure 8 demonstrates a gradual increase of the variability power from 14.5 GHz to 2–10 keV band (XRT observations), and afterward, the quantity $F_{\rm var}$ is declining with frequency. However, the *V*- and *R*-band data points depart from the general trend, showing larger fractional amplitudes than the higher-frequency UVOT bands. However, this is due to the more densely sampled optical observations with ground-based telescopes. As for the UVOT-band observations, in particular Periods 1–6, the quantity $F_{\rm var}$ did not show an increase with frequency in some periods (see Table 6). However, this exclusion can be partially related to the data sampling since some ObsIDs from these periods do not contain observations in all UV bands.

Although a limited sensitivity and the use of larger time bins can underestimate $F_{\rm var}$ values derived from the observations of some instruments, a double-peak shape in the $F_{\rm var}$–logν plane seems to be a characteristic feature of HBLs, and it has been reported by various authors for Mrk 421 from the MWL campaign performed in various epochs (Paper I; Alecsic et al. 2015b; Ahnen et al. 2016; Balocovic et al. 2016; Kapanadze et al. 2017a), for Mrk 501 in 2014 March–October (Kapanadze et al. 2017b), and for 1ES 1959+650 in different epochs (Kapanadze et al. 2016b, 2017c). A double-humped shape in the $F_{\rm var}$–logν plane, demonstrating the highest variability in the X-ray and VHE bands, was attributed to the correlation between the synchrotron and IC peaks by Furniss et al. (2015). Moreover, this shape can serve as an indication that the electron energy distribution is most variable at the highest energies (Alecsic et al. 2015b).

5.1.2. Flux Variability on Intraday Timescales

Our target was very active also on intraday timescales. We detected 113 instances of intraday 0.3–10 keV flux variability, including those with the shortest flux-doubling and halving times of about 1.20 hr. On 15 occasions, flux variability was observed within 1 ks observational runs (brightenings by 7%–24% in 180–720 s and declines by 6%–22% in 180–900 s). The corresponding duty cycle (i.e., the fraction of total observation time during which the object displayed 0.3–10 keV IDVs) was 43%, i.e., practically the same as in 2013 November–2015 June (Kapanadze et al. 2017a). Note that this value is considerably lower than those observed in 2005–2008 and 2013 January–May (about 84%; Kapanadze et al. 2017a, 2018). However, this result can be partially related to significantly more densely sampled campaigns in some parts of the latter periods. For example, Mrk 421 was observed very frequently during 2006 June 15–25, with a total exposure of 119 ks distributed over 124 XRT orbits. This was an unprecedented density of observations since the start of blazar monitoring with *Swift*, and it was more intense than the densest sampling in 2009–2012 (during 2009 May 22–27, presented in Section 4.4.2). In the period presented here, the source showed several flux-doubling and halving instances with $\tau_{\rm d} = 1.16$–23.80 hr and $\tau_{\rm h} = 1.20$–22.23 hr, respectively.

Figure 9 presents the quantity $f_{\rm var}$ as a function of the flux for the 0.3–10 keV IDVs that occurred in Mrk 421 during 2009–2012. We see that these events were observed at any

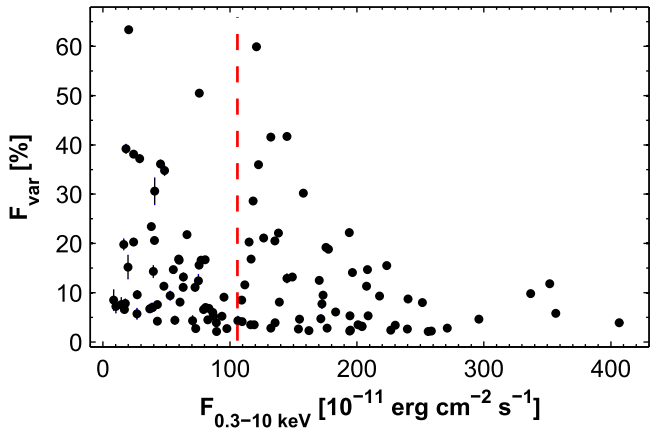

Figure 9. $F_{\rm var}$ values from the 0.3–10 keV IDVs plotted vs. unabsorbed 0.3–10 keV flux in 2009–2012. The vertical, red dashed line represents the mean value of the 0.3–10 keV flux.

brightness state, and a similar situation was also observed in 2013 January–May (Kapanadze et al. 2016a). During the periods 2005–2008 and 2015 January–June, the 0.3–10 keV IDVs were mostly observed in higher states, and the opposite situation was observed in 2013 November–2014 May (Kapanadze et al. 2017a, 2018). The IDVs observed during the flaring epochs can by triggered by the interaction of a propagating shock front with jet inhomogeneities; Sokolov et al. (2004). In contrast, the IDVs caused by other mechanisms occurring in the innermost blazar area should be more easily detectable in lower brightness states of the source when the variable emission from this area is not "shadowed" by the huge amount of the flux that is produced near the shock front (see, e.g., Kapanadze et al. 2014, 2016a, 2016b). We conclude that the importance of the flow disturbances occurring in the innermost AGN region and triggering 0.3–10 keV IDVs could be higher in 2013 November–2014 May, and these processes, along with the shock-in-jet scenario, may be at work in 2009–2012.

Along with the 0.3–10 keV flux, different spectral parameters showed variability on intraday timescales. However, these changes were not as fast as in 2005–2008 and 2013 January–May when these variations occurred even within 1 ks observational runs. For example, the spectrum softened/hardened by $\Delta a = 0.07$–0.10 in 330–500 s and the SED peaks showed shifts by 1.2–3.2 keV toward higher energies in 400–600 s. Sub-hour flux variability was also significantly more frequent in these periods, especially during the giant X-ray flare in 2013 April. We conclude that these differences could be related to significantly stronger turbulence in the jet area producing X-ray emission in these periods than in 2009–2012: the observational features associated with the stochastic acceleration in the turbulent jet area (discussed in Section 5.3.1) were more strongly featured by our target in these periods. Furthermore, a more frequent and faster flux/spectral variability in the periods 2005–2008 and 2013 January–May was possibly related to the stronger turbulence triggered by stronger shocks in the jet: a shock propagation can strongly amplify the turbulence in the shocked jet material, as predicted by the relativistic magnetohydrodynamic simulations of Mizuno et al. (2014). These simulations also showed that the higher-energy photons (including the X-ray ones) are more

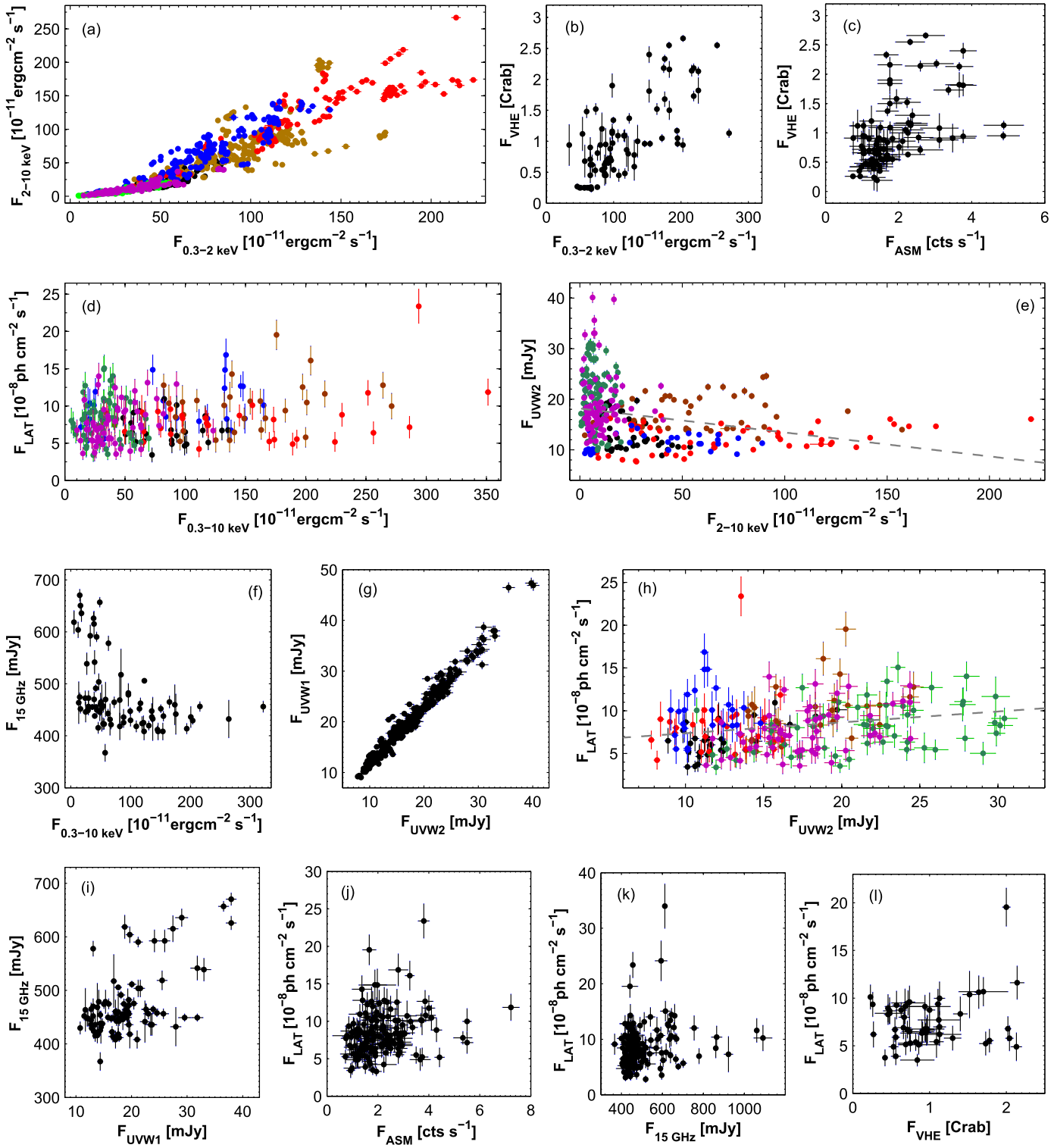

Figure 10. Correlations between multiband fluxes. The colored points in Figures 2(a)–(h) correspond to the different periods as follows: black corresponds to Period 1, brown to Period 2, red to Period 3, blue to Period 4, green to Period 5, and purple to Period 6. Gray dashed lines represent linear fits to scatter plots.

likely produced in the smallest jet areas with the highest magnetic field, which will depend on the shock strength. On the other hand, smallest-size emission zones can produce a very rapidly variable emission (based on the light-travel argument) that eventually should yield a more frequent detection of the sub-hour variability in the period that is characterized by stronger turbulence.

5.2. Interband Cross-correlations

5.2.1. Hard versus Soft X-Rays and Spectral Hysteresis

Similar to the previous years, the de-unabsorbed soft 0.3–2 keV and hard 2–10 keV fluxes were also strongly correlated during 2008–2009, although this correlation was significantly weaker in Period 2 (see Figure 10(a) and Table 9).

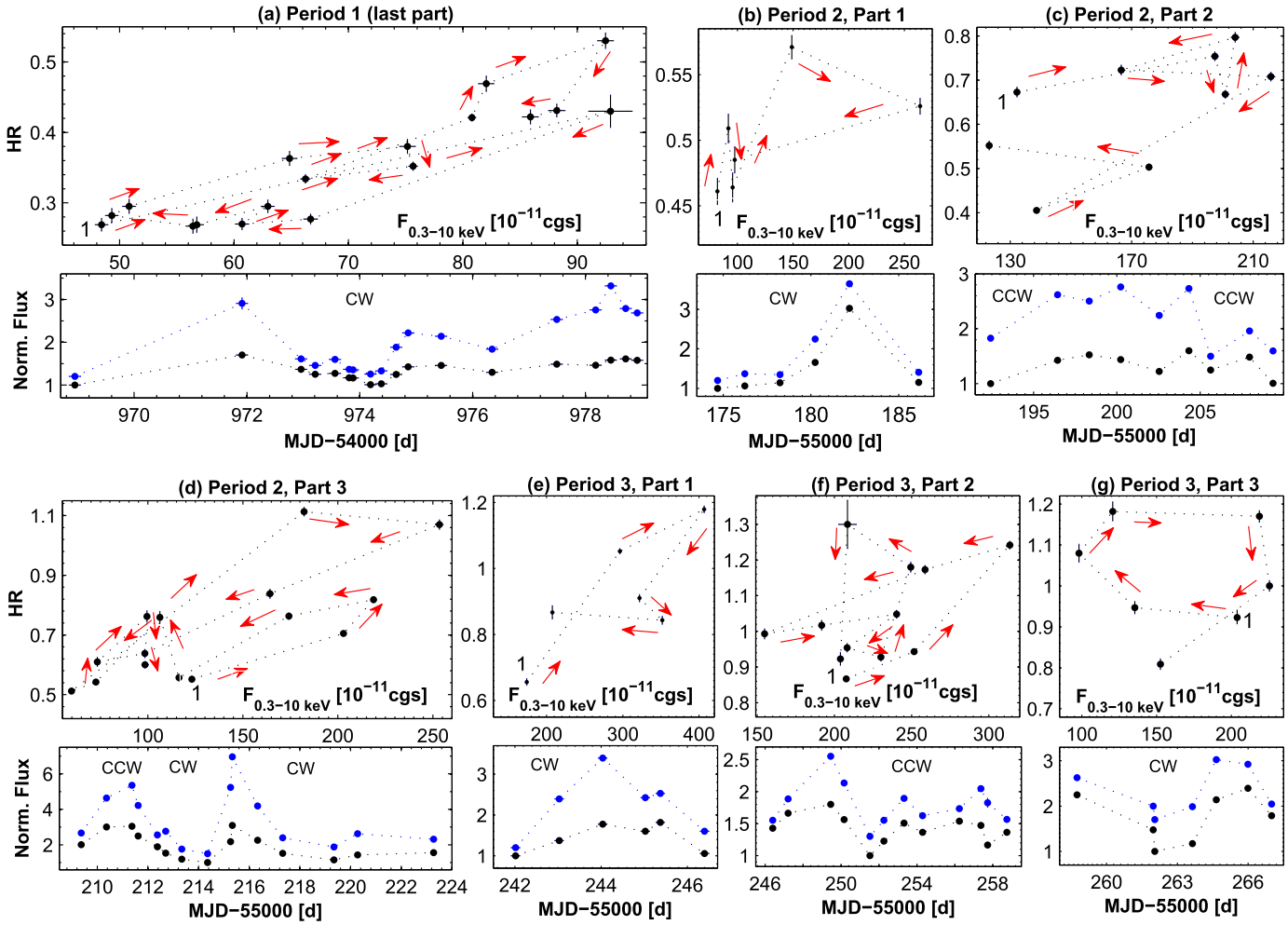

Figure 11. Spectral hysteresis in different epochs, along with normalized soft 0.3–2 keV (black points) and hard 2–10 keV (blue points) fluxes plotted as a function of time. The light curves for hard fluxes are shifted arbitrarily for better resolution. In each panel, the start point is denoted by "1." The abbreviation "cgs" stands for erg cm^{-2} s^{-1} (see the next page for Figures 11(l)–(n)).

Furthermore, Figure 10(a) demonstrates that the samples from Period 6 and some sub-samples from Periods 2–3 (producing outliers from the scatter plot) have different, smaller slopes than those from other periods, which may hint at different underlying physical conditions in the jet of Mrk 421 during these periods (see Tramacere et al. 2009 for the corresponding discussion).

Note also that the 2–10 keV flux showed a stronger variability than the soft one in each period (see Table 6 for the corresponding fractional amplitudes and the lower panels of Figures 11(a)–(b)). For example, the 0.3–2 keV flux varied by a factor of 20 in Period 2, while we observe a considerably stronger variability by a factor 85 in the 2–10 keV band. For the whole 2009–2012 period, a maximum-to-minimum flux ratio for the 2–10 keV flux $R \approx 503.2$, while $F^{\rm max}_{0.3-2{\rm keV}}/F^{\rm min}_{0.3-2{\rm keV}} = 49.4$ and this difference is significantly larger than those observed in 2005–2008 and 2013–2015 (see Table 8). Namely, in 2013 January–May (including the epoch of strongest X-ray flare since the start of the *Swift* monitoring of Mrk 41), $R_{0.3-2\,{\rm keV}} = 29.2$ and $R_{0.3-2\,{\rm keV}} = 136.3$, although the maximum 2-minute binned 0.3–10 keV count rate was twice higher than in the period presented here. However, the source showed significantly lower X-ray states in the latter period (1.9 cts s^{-1} versus 7.6 cts s^{-1}), and it was characterized by a wider range of the spectral index: $\Delta a = 1.51$ with $a_{\rm min} = 3.02$ in 2009–2012, while these quantities amounted to 1.15 and 2.83 in 2013 January–May. Note that 22 spectra in the period 2009–2012 (extracted from ObsID(30352)155,217,224) showed lower values of the parameter a than the hardest spectrum during the giant X-ray flare in 2013 April. However, these spectra were characterized by larger curvatures and an almost twice smaller height of the synchrotron SED peak $S_{\rm p}^{\rm max} = 1.3 \times 10^{-9}$ erg cm^{-2} s^{-1} versus $S_{\rm p}^{\rm max} = 2.5 \times 10^{-9}$ erg cm^{-2} s^{-1} in 2013 April) that eventually yielded significantly higher 0.3–2 keV and 2–10 keV fluxes in 2013 April. According to T09, the synchrotron SED peak height is related to the jet physical parameters as follows:

$$S_{\rm p} \propto N\gamma_{\rm p}^2 B^2 \delta^4, \quad (2)$$

with N the total emitter number, $\gamma_{\rm p}$ the peak of their distribution with energy, B the magnetic field strength, and δ the bulk Doppler factor of the jet emission zone. Lower photon indices of the aforementioned 23 spectra from the 2009–2012 period imply the presence of more higher-frequency X-ray photons in the 0.3–10 keV energy range. Since the synchrotron radiation peak frequency for a single particle can be given as $\nu_{\rm p} \sim \gamma^2 B$ (Massaro et al. 2006), the larger number of higher-frequency photons should be rather related to higher γ-values (and, hence, to larger $\gamma_{\rm p}$) than to the stronger magnetic field: the synchrotron

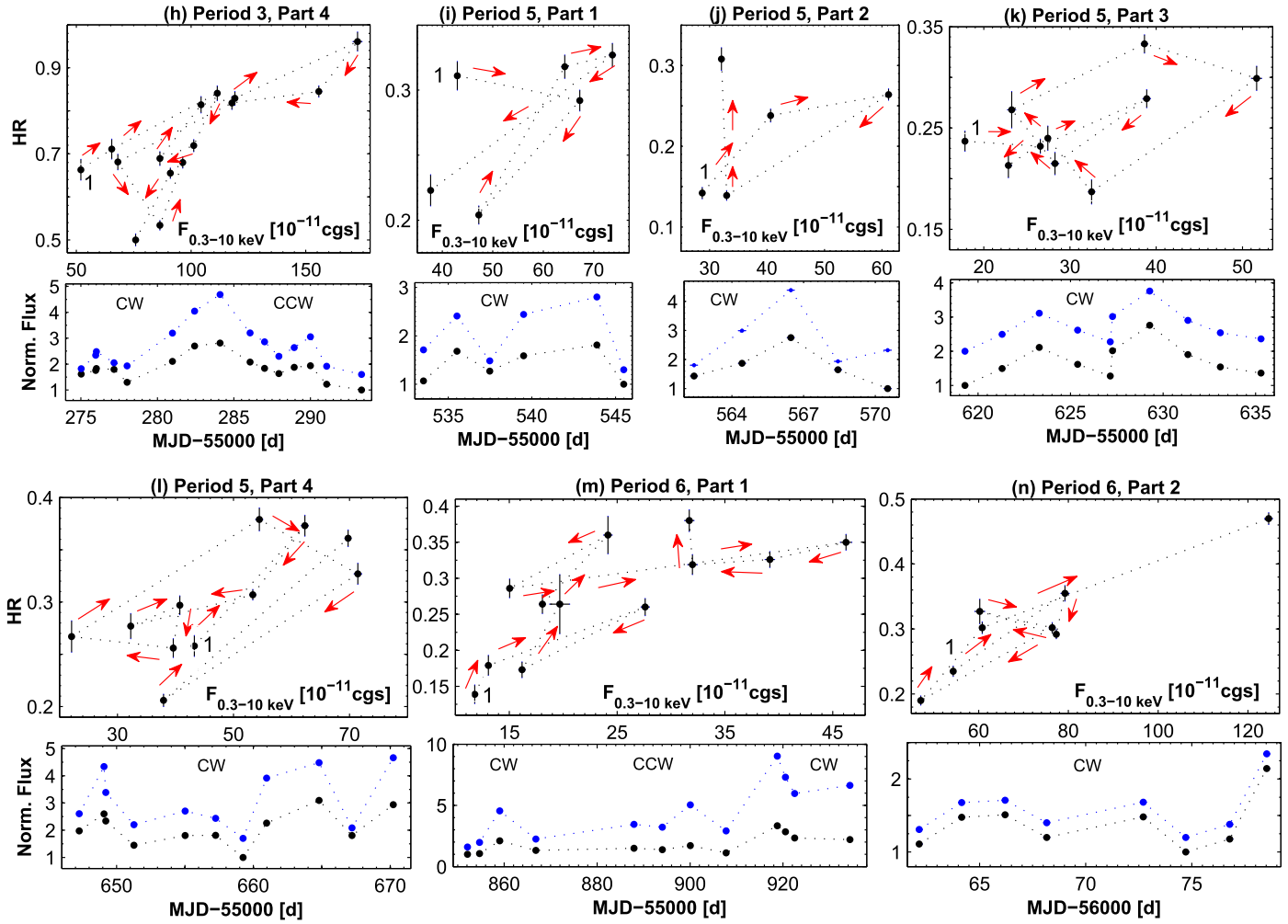

Figure 11. (Continued.)

emission coefficient is proportional to the latter as $j_{\nu}^{\rm syn} \sim B$ (see, e.g., Marscher 2014), and a stronger magnetic field would imply a higher synchrotron power produced by the emission zone (based on the assumptions that the emission zones had comparable sizes in both periods), which was observed in 2013 April. Note that HBL sources are not expected to have any significant contribution from the photons of the IC origin in the 0.3–10 keV energy range, especially in higher X-ray states when the aforementioned extreme values of the photon index were observed. Finally, the significantly higher $S_{\rm p}$ values and X-ray fluxes in 2013 April were probably due to higher values of the quantities N, B, and δ compared to the 2009–2012 period.

The difference in the variability strength in the soft and hard X-rays led to the extreme spectral variability of Mrk 421 on diverse timescales, which was discussed in detail in Section 4. In that case, the presence of hard ($\tau_{\rm hard}$) or soft ($\tau_{\rm soft}$) delays (i.e., the flares in 2–10 keV energy range lead those in the 0.3–10 keV band and vice versa, respectively) are expected. However, short XRT observations with much longer intervals between them do not allow deriving the values of the soft or hard delays by means of the commonly used techniques (e.g., the local cross-correlation function; Max-Moerbeck et al. 2014). Furthermore, the strong X-ray spectral variability in Mrk 421 in the period presented here led to the development of "loops" in the HR–flux plane during some flares (Figure 11), which allows us to draw conclusions about the interplay of the acceleration ($\tau_{\rm acc}$), synchrotron cooling ($\tau_{\rm syn}$), and flux variability ($\tau_{\rm var}$) timescales in the jet emission zone. In particular, when $\tau_{\rm syn} \gg \tau_{\rm var} \gg \tau_{\rm acc}$ (or $\tau_{\rm syn} \gg \tau_{\rm acc} \gg \tau_{\rm var}$), the spectral evolution should be due to the flaring component starting in the hard X-ray band, triggered by a rapid injection of very energetic particles (Tramacere et al. 2009). In that case, the spectrum is expected to become progressively harder in the flux increase phase and softer along with brightness decline, resulting in a clockwise (CW) "movement" of the source in the HR–flux plane. Such spectral evolution of MRK 421 in some intervals of Periods 1–3 and 5–6 (see Figures 11(a), (b), (d), (e), (g)–(k), and Table 10 for details), implying that the hard X-ray variability led that in the soft X-rays both during the increase and the decrease of brightness, i.e., the source should have soft lags in those cases (Cui 2004). In fact, the lower panels of the corresponding plots indicate a possible soft lag at MJD(549)73,75,78 (Period 1, Figure 11(a)), MJD(55)244,264 (Period 3, Figures 11(e), (g)) etc. CW-type spectral patterns have often been reported for our target from the XRT observations performed in 2005–2008 and 2013 January–2015 June (T09; Kapanadze et al. 2016a, 2017a, 2018), as well as from the campaigns with other space missions (see

Table 9
Correlations between Multiband Fluxes (Denoted by "F_i" for the Particular i band) in Different Periods

Quantities	ρ 2005–2008	p
$F_{0.3-2\ \mathrm{keV}}$ and $F_{2-10\ \mathrm{keV}}$	0.87(0.03)	$<10^{-15}$
$F_{0.3-10\ \mathrm{keV}}$ and F_{VHE}	0.63(0.07)	8.00×10^{-11}
F_{ASM} and F_{VHE}	0.52(0.09)	2.19×10^{-9}
$F_{2-10\ \mathrm{keV}}$ and F_{UVW2}	−0.32(0.10)	8.09×10^{-6}
$F_{2-10\ \mathrm{keV}}$ and F_{UVM2}	−0.31(0.10)	3.44×10^{-5}
$F_{2-10\ \mathrm{keV}}$ and F_{UVW1}	−0.34(0.10)	4.51×10^{-6}
$F_{0.3-10\ \mathrm{keV}}$ and $F_{15\ \mathrm{GHz}}$	−0.51(0.08)	8.89×10^{-8}
F_{UVW1} and F_{UVM2}	0.94(0.02)	$<10^{-15}$
F_{UVW1} and F_{UVW2}	0.95(0.02)	$<10^{-15}$
F_{UVM2} and F_{UVW2}	0.95(0.02)	$<10^{-15}$
F_{UVW2} and F_{LAT}	0.23(0.10)	4.51×10^{-3}
F_{UVW1} and $F_{15\ \mathrm{GHz}}$	0.42(0.09)	7.11×10^{-7}
F_{UVM2} and $F_{15\ \mathrm{GHz}}$	0.40(0.10)	3.40×10^{-6}
F_{UVW2} and $F_{15\ \mathrm{GHz}}$	0.41(0.10)	1.29×10^{-6}
F_{ASM} and F_{LAT}	0.27(0.11)	2.19×10^{-3}
F_{LAT} and $F_{15\ \mathrm{GHz}}$	0.26(0.12)	7.20×10^{-3}
Per 1		
$F_{0.3-2\ \mathrm{keV}}$ and $F_{2-10\ \mathrm{keV}}$	0.83(0.03)	$<10^{-15}$
$F_{2-10\ \mathrm{keV}}$ and F_{UVW2}	−0.37(0.08)	2.92×10^{-7}
$F_{2-10\ \mathrm{keV}}$ and F_{UVM2}	−0.36(0.08)	7.02×10^{-6}
$F_{2-10\ \mathrm{keV}}$ and F_{UVW1}	−0.37(0.10)	4.00×10^{-6}
F_{UVW2} and F_{LAT}	0.39(0.12)	1.33×10^{-5}
Per 2		
$F_{0.3-2\ \mathrm{keV}}$ and $F_{2-10\ \mathrm{keV}}$	0.68(0.05)	6.35×10^{-8}
F_{UVW2} and F_{LAT}	0.45(0.10)	3.41×10^{-7}
Per 3		
$F_{0.3-2\ \mathrm{keV}}$ and $F_{2-10\ \mathrm{keV}}$	0.85(0.03)	$<10^{-15}$
$\log E_{\mathrm{p}}$ and $\log S_{\mathrm{p}}$	0.31(0.12)	8.77×10^{-4}
Per 4		
$F_{0.3-2\ \mathrm{keV}}$ and $F_{2-10\ \mathrm{keV}}$	0.82(0.03)	$<10^{-15}$
Per 5		
$F_{0.3-2\ \mathrm{keV}}$ and $F_{2-10\ \mathrm{keV}}$	0.90(0.02)	$<10^{-15}$
F_{UVW2} and F_{LAT}	0.34(0.11)	4.44×10^{-5}
Per 6		
$F_{0.3-2\ \mathrm{keV}}$ and $F_{2-10\ \mathrm{keV}}$	0.89(0.03)	$<10^{-15}$
$F_{0.3-10\ \mathrm{keV}}$ and F_{VHE}	0.28(0.11)	8.99×10^{-3}
$F_{0.3-10\ \mathrm{keV}}$ and F_{LAT}	0.33(0.11)	5.22×10^{-4}
F_{UVW2} and F_{LAT}	0.35(0.12)	7.01×10^{-4}

Note. For each correlation, ρ and p denote the Spearman coefficient and the corresponding p-chance.

Brinkmann et al. 2001; Cui 2004; Ravasio et al. 2004; Rebillot et al. 2006; Acciari et al. 2009).

The source showed the opposite, counterclockwise (CCW) spectral activity relatively rarely during 2009–2012, and they were observed in some intervals of Period 2–3 and 6 (see Figures 11(c), (d), (f), (h), and (m)). In the case of CCW-type evolution, $\tau_{\mathrm{syn}} \approx \tau_{\mathrm{acc}} \approx \tau_{\mathrm{var}}$, i.e., the particles are gradually accelerated, while the brightness decline epoch can be dominated by the particle escape effects, and we therefore should observe a hard lag (Ravasio et al. 2004). The corresponding 0.3–2 keV and 2–10 keV light curves show possible hard lags at MJD (55)196,200,211 (Period 2, Figures 11(c) and (d)), MJD(552) 48, 57 (Period 3, Figure 11(f)) etc. Similar results were also reported in past X-ray spectral studies of Mrk 421 (Cui 2004; Kapanadze et al. 2016a, 2017a, 2018; T09 etc.).

In contrast to the periods 2005–2008 and 2013 January–May, hysteresis patterns were not seen on intraday timescales during the 2009–2012 observations. No clear patterns were evident either during Period 5, most of Period 1, and some parts of other periods. This feature could be related to the emergence of different flaring components with different interplays between electron acceleration, synchrotron cooling, and flux variability timescales that prevented the generation of a dominant CW- or CCW-type spectral evolution during the X-ray variability observed in these epochs. This result is in agreement with the fact that the period presented here does not show a dominant physical factor for the observed spectral variability from the correlation $S_{\mathrm{p}} \propto E_{\mathrm{p}}^{\alpha}$ (based on the assumption about the synchrotron emission from one dominant homogenous component; see Section 5.3.1).

5.2.2. X-Rays versus HE-VHE and Radio–UV Emissions

Figure 10(b) shows a medium positive correlation between the 0.3 and 10 keV and VHE fluxes during 2009–2012 (see Table 9). Moreover, a positive but relatively weak $F_{1.5-12\ \mathrm{keV}}$–$F_{\mathrm{VHE\ keV}}$ correlation was also revealed (Figure 10(c)). Simultaneous X-ray–TeV flares occurred in the periods discussed in Section 4 when the VHE data were available (Periods 1–3). This result is in agreement with the one-zone SSC scenario, although the latter may not be applicable in the second part of Period 3, when the strongest TeV flare during 2009–2012 was observed in the epoch when the source showed a low-amplitude 0.3–10 keV variability, superimposed on a long-term declining trend (corresponding to the lower right outliers from the scatter plots in Figures 10(b)–(c)). This instance corresponds to more than a quadratic relation between the X-ray and VHE fluxes, which cannot be achieved in the case of upscatter of the synchrotron photons in the Thomson regime (and is even less expectable in the Klein–Nishina (K–N) regime, yielding a linear relation between these emissions; see Aharonian et al. 2009). Note that we reported the instances of uncorrelated X-ray–VHE variability also from our past studies of Mrk 421. Namely, the source twice underwent strong XRT/ASM/BAT-band flares in 2006–2008 when it was not detected with 3σ significance in the TeV band, or strong VHE flares were recorded in the epochs of low X-ray states (Paper I). Several occasions of uncorrelated XRT and VHE variability were observed in 2013 November–2015 June when the source was monitored with FACT (Kapanadze et al. 2017a): strong, fast VHE flares by factor of 7–13, without or with non-comparable X-ray brightenings. Conversely, the source was not detectable by FACT or showed a low TeV state during the three X-ray flares, or there were some time shifts between the flares in these bands, which is difficult to explain by the one-zone SSC scenario (Blazejowski et al. 2005).

During the whole 2009–2012 period, the source showed a very weak positive correlation between the 0.3 and 10 keV and 0.3–300 GeV fluxes, which was relatively stronger in Period 6. The LAT-band flux was also correlated very weakly with the ASM-, UVOT- and radio-band fluxes (see Figures 10(d), (h),

Table 10
List of CW- and CCW Loops Shown by Mrk 421 in the HR–flux Plane

Figure	MJD	Variability Instance
		CW-evolution
11(a)	54968.9–54978.9	Two fast low-amplitude flares at the end of Period 1 (see Figure 4(a))
11(b)	55174.7–55186.1	A fast flare in the middle of Period 2 (Figure 4(b))
11(d)	55212.7–55223.7	The last flare in Period 2 (Figure 4(b))
11(e)	55242.0–55246.4	A fast flare in Period 2, encompassing the highest X-ray states during 2009–2012 (Figure 4(c))
11(g)	55258.7–55267.1	Fast flares superimposed on long-term declining trend in Period 3 (Figure 4(c))
11(h)	55275.0–55287.0	The last flare in Period 3 (Figure 4(c))
11(i)	55533.5–55545.5	The first flare in Period 5 (Figure 4(e))
11(j)	55562.4–55570.5	A fast flare superimposed on the second long-term flare in Period 5 (Figure 4(e))
11(k)	55619.3–55635.3	A low-amplitude flare superimposed on the long-term flare in the middle of Period 5 (Figure 4(e))
11(l)	55647.3–55670.2	Fast low-amplitude flares in the highest brightness epoch in the middle of Period 5 (Figure 4(e))
11(m)	55852.1–55887.9	Minor fluctuations in the lowest brightness epoch in Period 6 (Figure 4(f))
11(m)	55918.8–55934.4	The first low-amplitude flare after the lowest X-ray states in Period 6 (Figure 4(f))
11(n)	56062.0–56079.0	The epochs of highest brightness states at the end of Period 6 (Figure 4(f))
		CCW-evolution
11(c), (d)	55192.4–55212.4	Low-amplitude flares in the second half of Period 2 (Figure 4(b))
11(f)	55246.4–55258.7	Low-amplitude flares in the middle of Period 3 (Figure 4(c))
11(h)	55287.0–55293.3	The last minor fluctuation in Period 3 (Figure 4(c))
11(m)	55894.0–55918.8	Minor fluctuations in the lowest brightness epoch in Period 6 (Figure 4(f))

Note. See the top panel of each figure cited in the last column.

(k), and Table 9).[15] This result can be related to the IC uppscatter of the radio–UV fluxes to MeV–GeV energies in the Thomson regime and the upscatter of X-ray ones to the same energy range in the K–N regime. Possibly, the presence of both processes leads to a weakness in the aforementioned correlations.

We have found an anticorrelation between the contemporaneous X-ray and radio–UV observations (see Figures 10(e), (f)). Note that Figure 4 demonstrates a mostly "independent" and longer-term radio–UV variability of the source in different periods, with a low state or long-term declining trend, along with several X-ray flares. A similar situation was reported by us for some intervals from the periods 2005–2008 and 2013 November–2015 June (see Kapanadze et al. 2017a, 2018) and this feature was explained through a hardening of the electron energy distribution that can shift the entire synchrotron bump to higher energies. During this process, the emission at the rising segment of the synchrotron SED (radio–UV) would decrease, while that on the decreasing segment (X-rays) would increase (Alecsic et al. 2015a). Our finding of a positive $E_{\rm p}$–$F_{0.3-10\ {\rm keV}}$ correlation (see Section 3.3), i.e., a shift of the synchrotron SED peak toward higher energies with the increasing X-ray flux, also favors this explanation. The simulations of Virtanen & Vainio (2005) yielded that the stochastic acceleration behind the shock relativistic front can lead to the gradual shift of the whole particle spectrum to higher energies. Note that the shift of the peak of electron energy distribution with higher brightness was also predicted by the simulations of Katarzynski et al. (2006) in the framework of the stochastic acceleration of electrons with a narrow initial energy distribution that is characterized by a considerably higher average energy than the equilibrium energy.

[15] Carnerero et al. (2017) reported a positive correlation of the near-IR, UV, and HE variability of Mrk 421 with the optical one from the data sets obtained during 2007–2015.

Finally, Figure 10(g) demonstrates that the UVOT-band fluxes showed very strong correlations in all periods (see also Table 4) and did not exhibit any features (e.g., a significant variability of the color index $m_{\rm UVW1}$–$m_{\rm UVW2}$, where $m_{\rm UVW1}$ and $m_{\rm UVW2}$ are the UVW1- and UVW2-band magnitudes), indicating that these emissions are produced by different electron populations.

5.3. The Ranges of Spectral Parameters and Related Physical Processes

5.3.1. Spectral Curvature

The parameter b mostly showed relatively low values in 2009–2012: the mean value $\overline{b} = 0.27$ and 95% of the log-parabolic spectra yielded $b < 0.4$. However, even lower values were observed in 2005–2008, 2013 January–May and 2013 November–2014 May with $\overline{b} = 0.21$–0.25 and with a higher percentage of the spectra with $b \geqslant 0.20$ (43%–57% versus 25% in 2009–2012). Note that relatively low curvatures (i.e wide synchrotron SEDs) are predicted in the case of stochastic acceleration (second-order Fermi mechanism) of the emitting particles, which can arise from magnetic turbulence close to the shock front (Massaro et al. 2011b; Tramacere et al. 2009, hereafter T09). Therefore, we conclude that the stochastic processes could be important for the production of the X-ray emission in the jet of Mk 421 during the period presented here that agree with the detected b–$E_{\rm p}$ anticorrelation that is expected in the case of efficient stochastic acceleration (Tramacere et al. 2009). Note that Massaro et al. (2011a) demonstrated that the electrons in the jets of TeV-detected HBLs (TBLs) should undergo a more efficient stochastic acceleration than in those of the TeV-undetected HBLs, and this prediction is in agreement with our findings. Moreover, the anticorrelation between the 0.3 and 10 keV and radio–UV variabilities that is observed for our target in some intervals of the 2009–2012 period is explained in the framework of the

Table 11
The Ranges of Spectral Parameters in HBLs During 1997–2016

Source (1)	Z (2)	a (3)	Γ (4)	b (5)	E_p (6)	Reference (7)
Mrk 421	0.031	1.34(0.02)-3.02(0.06)	1.68(0.02)-2.75(0.03)	0.06(0.02)-0.64(0.06)	0.02(0.01)-22.39(2.02)	R04,K18a,TW
Mrk 501	0.034	1.39(0.06)-2.05(0.05)	1.54(0.02)-2.22(0.04)	0.12(0.01)-0.56(0.11)	0.49(0.03)-101.6(23.7)	K17b,M08
1ES 1959+650	0.048	1.46(0.05)-2.37(0.03)	1.71(0.02)-2.22(0.01)	0.12(0.04)-0.98(0.12)	0.12(0.04)-12.80(0.75)	K16b,K16c
PKS 2155−304	0.116	2.04(0.02)-2.75(0.02)	2.51(0.02)-2.81(0.02)	0.11(0.02)-0.80(0.15)	0.02(0.01)-0.89(0.10)	M08,K14
PG 15553+113	>0.4	2.17(0.07)-2.21(0.03)	2.09(0.03)-2.21(0.02)	0.23(0.04)-0.63(0.08)	0.51(0.11)-0.73(0.11)	M08
1ES 1011+496	0.212	1.72(0.04)-2.48(0.06)	1.94(0.05)-2.50(0.07)	0.10(0.04)-0.67(0.20)	0.13(0.04)-5.01(0.68)	M08,K15
H 1426+428	0.129	1.68(0.02)-1.97(0.02)	1.86(0.03)-2.22(0.11)	0.12(0.02)-0.49(0.10)	1.11(0.06)-21.95(0.60)	M08
H 1515+660	0.701	1.27(0.10)-2.17(0.06)	1.58(0.07)-2.53(0.18)	0.12(0.08)-0.89(0.22)	1.34(0.67)-3.53(1.52)	K15
PKS 2005−489	0.071	1.96(0.05)-3.12(0.02)	2.00(0.03)-3.14(0.04)	−0.23(0.06)-0.70(0.34)	0.36(0.20)-1.25(0.22)	M08,K15
PKS 0548−322	0.069	1.53(0.07)-1.87(0.05)	1.49(0.03)-2.40(0.14)	0.14(0.03)-0.52(011)	1.77(0.21)-4.13(0.47)	M08, K15
1ES 0120+340	0.272	1.39(0.20)-1.94(0.14)	1.69(0.19)-1.94(0.14)	0.33(0.22)-1.28(0.38)	1.46(0.24)-3.31(0.44)	M11a, K15
1ES 1218+304	0.184	1.89(0.05)-2.25(0.06)	1.97(0.06)-2.25(0.06)	0.39(0.11)-0.46(0.06)	0.63(0.08)-1.32(0.16)	M08
1ES 2344+514	0.044	1.36(0.08)-1.87(0.11)	1.72(0.01)-2.27(0.04)	0.36(0.19)-0.83(0.33)	1.35(0.36)-6.03(0.89)	M08,K17c
RBS 30	0.095	1.83(0.06)-1.89(0.05)	⋯	0.36(0.19)-0.68(0.15)	1.24(0.11)-1.44(0.29)	M11a
1ES 1421+582	0.638	1.91(0.07)-1.98(0.10)	1.77(0.10)-2.22(0.18)	0.37(0.17)-0.59(0.30)	1.22(0.33)-1.42(0.30)	K15
1ES 0033+595	0.467	0.93(0.05)-1.60(0.16)	⋯	0.36(0.07)-0.93(0.07)	3.59(0.85)-6.47(0.95)	W16
1ES 1727+502	0.055	1.76(0.06)-2.12(0.08)	1.90(0.05)-2.39(0.08)	0.28(0.14)-0.65(0.18)	0.81(0.14)-1.37(0.19)	M11a,K15
RGB J0710+591	0.125	1.62(0.06)-1.73(0.06)	1.60(0.04)-1.85(0.02)	0.17(0.11)-0.23(0.13)	6.22(0.85)-6.70(0.93)	K15
1ES 1101−232	0.186	1.64(0.08)-2.04(0.02)	1.95(0.09)-1.99(0.10)	0.17(0.03)-0.40(0.05)	0.76(0.06)-3.50(0.33)	M08,K15
1ES 0229+200	0.140	1.45(0.10)-1.60(0.10)	1.43(0.06)-1.45(0.06)	0.31(0.08)-0.44(0.21)	4.22(0.47)-5.54(0.65)	M08,K15
1ES 0502+675	>0.3	1.63(0.11)-1.91(0.06)	–	0.28(0.13)-0.70(0.20)	1.28(0.18)-2.17(0.26)	K15
Mrk 180	0.045	1.60(0.06)-2.71(0.08)	1.96(0.05)-2.59(0.07)	0.17(012)-0.66(0.30)	0.29(0.07)-8.11(0.85)	M08,K15
RBS 1004	0.134	1.47(0.07)-1.74(0.07)	⋯	0.38(0.19)-0.96(0.23)	1.54(0.16)-4.26(1.57)	M11a,K15
RBS 76	0.610	2.11(0.05)-2.30(0.09)	2.13(0.13)-2.29(0.09)	0.49(0.21)-0.79(0.13)	0.49(0.16)-0.79(0.13)	K15
BZBJ1137−1710	0.601	1.39(0.11)-1.67(0.13)	1.48(0.15)-1.84(0.12)	0.75(0.24)-1.09(0.39)	1.42(0.58)-2.55(0.67)	K15
RBS 1457	>0.5	1.47(0.12)-1.73(0.11)	1.75(0.17)-2.19(0.16)	0.74(0.28)-1.19(0.27)	1.52(0.46)-1.67(0.48)	K15
1ES 1533+535	0.875?	2.00(0.09)-2.22(0.06)	⋯	0.34(0.18)-0.65(0.28)	0.47(0.11)-1.00(0.29)	K15
BZBJ1341+3959	0.169	1.55(0.09)-1.64(0.07)	⋯	0.66(0.21)-0.70(0.14)	1.82(019)-2.20(0.38)	M11a
RBS 1366	0.236	1.72(0.15)-2.03(0.11)	1.90(0.09)	0.39(0.34)-0.88(0.59)	0.94(0.21)-2.08(1.24)	M11a
1ES 1440+122	0.163	1.80(0.20)-1.83(0.11)	2.15(0.18)	0.32(0.16)-1.36(0.57)	1.18(0.15)-1.93(0.52)	M11a
B3 2247+381	0.119	1.80(0.09)-2.43(0.06)	2.38(0.07)	1.22(0.13)-0.29(0.18)	0.19(0.02)-1.33(0.12)	M11a
BZBJ0832+3300	0.672	1.47(0.13)-1.52(0.07)	1.29(0.09)-1.81(0.09)	0.37(0.15)-0.87(0.31)	2.02(0.30)-4.45(0.52)	K15

Note. The references in Column (7) are as follows: R04, Ravasio et al. (2004); TW, this work; K17b, Kapanadze et al. (2017b); K16b, Kapanadze et al. (2016b); K16c, Kapanadze et al. (2016c); K14, Kapanadze et al. (2014); K15, Kapanadze et al. (2015); M11a, Massaro et al. (2011a); K17c, Kapanadze et al. (2017d); and W16, Wierzcholska & Wagner (2016).

stochastic acceleration (see Section 5.2.2). However, the b–E_p anticorrelation was weak (or very weak) in different periods, which can be explained as due to "contamination" of stochastic acceleration of the electrons by cooling and other types of acceleration (Kapanadze et al. 2016b).

Table 11 demonstrates that Mark 421 and Mrk 501 have shown one of the lowest spectral curvatures among the well-studied bright HBLs that might be related to the stronger turbulence and more efficient stochastic acceleration in the jets of these sources. Although some other HBLs (e.g., H 1426 +428, RGB J0710+591, and 1ES 1101−232) are characterized by low spectral curvatures, they have been little studied, and we are not able to draw a statistically significant conclusion about the importance of the stochastic acceleration in these sources.

Another plausible mechanism for the establishment of a curved energy spectrum of X-ray emitting electrons is the so-called energy-dependent acceleration probability process (EDAP; see M04) at a shock front by the first-order Fermi mechanism in a medium where the electrons are confined by a magnetic field with a confinement efficiency that decreases with increasing gyroradius (see Massaro et al. 2004 and Paper I for details). In the framework of EDAP, a positive correlation between the parameters a and b is expected, which was observed in 2009–2012, although this correlation was very weak; this indicates other types of acceleration mechanisms, e.g., stochastic acceleration in the shocked jet area, which does not yield the a–b correlation. For example, the particle can be accelerated at the shock front by the first-order Fermi process and continue to gain additional energy via the stochastic mechanism into the shock downstream region. Eventually, particle will be able to re-enter the shock acceleration region after gaining sufficient energy, and and repeat the aforementioned acceleration cycle (Katarzynski et al. 2006).

The positive a–b correlation was stronger for our target during the XRT observations of our target in 2015 February (a medium correlation with $\rho = 0.57$). An even stronger correlation was reported by Massaro et al. (2004) from the *BeppoSAX* observations in 1997–1999. Other bright HBLs (1ES 1959 +650, Mrk 501, and PKS 2155−304) have not exhibited evidence of EDAP (see Kapanadze et al. 2014, 2016b, 2016c, 2017b, 2017c).

During 2009–2012, the source showed a considerably higher occurrence of log-parabolic spectra compared to the 2005–2008 period (93.3% versus 72.5%), and this finding can be related to a more frequent absence of the first- and second-order Fermi processes during the XRT observations performed in the latter period. In 2009–2012, several XRT

observations of Mrk 421 revealed an extreme spectral variability: in each case, the source twice showed a transition from the log-parabolic into a power-law spectrum and vice versa, with 1 ks observational run. These instances hint at the extremely rapid changes of the magnetic field properties in the emission zone: from the state with a decreasing confinement efficiency with increasing gyroradius (or from the turbulent state, both yielding a log-parabolic spectrum) into that without these properties (power-law spectrum), and vice versa.

5.3.2. The Position of the Synchrotron SED Peak

Our X-ray spectral study of Mrk 421 has revealed an extreme variability of the parameter E_p during 2009–2012. In lower X-ray states, the synchrotron SED peak was situated at energies as low as a few eV, while the source was a hard X-ray peaking HBL (i.e., $E_p > 2$ keV on 173 occasions, which amounts to 19% of all log-parabolic spectra). In this period, the source showed a higher percentage of hard X-ray peaking spectra, and the maximum value of E_p was higher than during the strongest X-ray flares in 2013 April (13% of all log-parabolic spectra showing $E_p > 2$ keV with the highest value of 10 keV; Kapanadze et al. 2016a). During 2013 November–2015 June, the source showed $E_p^{max} = 9.15$ keV, and only 5% of the log-parabolic spectra yield $E_p > 2$ keV (Kapanadze et al. 2017a). At least 94 spectra had their syncrotron peaks at UV frequencies: the corresponding E_p values are lower than 0.1 keV (a conventional threshold between the UV and X-ray energy ranges), and even more spectra from this period could be the UV-peaking HBLs since the E_p values below 0.8 keV generally are upper limits to the intrinsic position of the synchrotron SED peak.

Note that Mrk 421 was characterized by more extreme spectra in 2005 March–2008 June than in the period presented here: $E_p^{max} = 22.4$ keV (the only period with a possible position of the synchrotron SED peak beyond 20 keV), and the source was a hard X-ray peaking HBL on 205 occasions (amounting to 24% of all log-parabolic spectra; Paper I.) Moreover, the variability of E_p in Mrk 421 was relatively less extreme than that exhibited by Mrk 501 during the dramatic X-ray flare in 1997 April, when the position of the synchrotron SED moved from 0.94 keV to beyond 100 keV (Tavecchio et al. 2001). Mrk 501 also showed a large shift from 0.79 keV to 21.96 keV during the strong X-ray activity in 2014 March–October, and 95% of these spectra showed $E_p > 2$ keV and a distribution peak at 3.45 keV (Kapanadze et al. 2017b). As for other HBLs, the widest overall ranges of E_p during 1997–2016 were shown by 1ES 1959+650, 1ES 1011+496 and H 1426 +428 (corresponding to $\Delta \log \nu_p \sim$ 1.3–2.0 orders of the frequency; see Table 11). Other HBLs have shown significantly smaller ranges than one order, but they are still little studied.

Note that the source showed a positive E_p–$F_{0.3-10\,keV}$ correlation, i.e., the synchrotron SED peak showed a shift toward higher frequencies with increasing flux during X-ray flares, and vice versa. However, the weakness of the correlation implies that the source did not follow this trend during all flares. Namely, no significant correlation was revealed for Period 2, and we cannot draw conclusions about Periods 1 (due to very few spectra with peaks at energies above 0.8 keV), or due to the absence of E_p values above this threshold (Periods 5–6). A similar situation was observed in 2005–2008 and 2013 January–May, while no significant E_p–$F_{0.3-10\,keV}$ correlation was found in 2013 November–2015 June (Kapanadze et al. 2016a, 2017a, 2018). This trend was stronger in 1ES 1959+650 during 2015 August–2016 August (Kapanadze et al. 2016b, 2017c) and in Mrk 501 in 2014 March–October (Kapanadze et al. 2017b).

In the framework of the synchrotron emission mechanism from one dominant homogenous component, the detection of the correlation $S_p \propto E_p^{\alpha}$ allows us to draw a conclusion about the physical factor that makes the main contribution to the observed spectral variability of the source, depending on the values of the exponent α (ranging between 0.6 and 4; Massaro et al. 2008; Tramacere et al. 2011). Figure 2(e) presents a positive S_p–E_p correlation during 2009–2012 with the exponent $\alpha = 0.33 \pm 0.08$. This correlation was observed in Periods 2 and 3 separately with $\alpha = 0.37 \pm 0.11$ and $\alpha = 0.27 \pm 0.10$, respectively. Note that these values are outside the aforementioned range when the spectral variability is driven by some dominant physical factor. We conclude that the extreme spectral variations in our target, observed during 2009–2012, were triggered by the underlying complex and variable physical conditions, with no dominant factor. Moreover, the jet emission zone probably was not suitable for the assumption of having one dominant homogenous component (adopted to derive the aforementioned relation) in the period presented here.

A weak positive S_p–E_p correlation was observed during the period 2005 March–2008 June, and the sample of the spectra from 2008 April–June showed a value of the exponent $\alpha = 0.52$ (Kapanadze et al. 2017a), which is close to $\alpha = 0.6$, implying that the main driver of the observed spectral changes is the variability of the parameters D_p (the momentum-diffusion coefficient) and q (the exponent describing the turbulence spectrum; namely, a transition from the Kraichnan-type into the "hard sphere" spectrum) during the stochastic acceleration of the particles (Tramacere et al. 2011). A similar result was reported from the XRT observations of our target performed during 2008 April–June (Paper I), as well as for 1ES 1959+650 (2016 January–August; Kapanadze et al. 2017c) and Mrk 501 (2014 March–October; Kapanadze et al. 2017c).

5.3.3. Photon Index and Hardness Ratio

An extreme spectral variability of our target in 2009–2012 was reflected in a very wide range of the photon index. In the low X-ray states, the log-parabolic spectra were very soft, with the photon index at 1 keV exhibiting a maximum value $a = 3.03$, which is the historically highest value for this source. In other periods, Mrk 421 showed $a_{max} = 2.63$–2.83 in 2005–2008, 2013 January–May, and 2013 November–2015 June (see Paper I and Kapanadze et al. 2016a, 2017a). Note that the spectra with $a \geqslant 3$ are observed very rarely for HBLs and have been reported only for PKS 2005–489 (see Table 11).

On the other hand, the source exhibited very hard 0.3–10 keV spectra during the strong X-ray flares observed in Periods 2–3. In the study presented here, we have revealed 27 spectra with $a = 1.51$–1.69, which have rarely been reported for HBLs. The hardest spectrum in 2005–2008 was described with $a_{min} = 1.62$ (Paper I), and this quantity was equal to 1.68 and 1.75 during the giant X-ray flare in 2013 April and in the period 2013 November–2015 June, respectively (Kapanadze et al. 2016a, 2017a). On the other hand, the harder spectra with $a = 1.34$–1.45 were reported by Ravasio et al. (2004) from the

two *XMM-Newton* observations on 2002 November 4. Furthermore, more extreme results were reported for 1ES 1959+650 with 88%–95% of spectra harder than $a = 2$ and 49 spectra with $a = 1.46$–1.69 in Kapanadze et al. (2016b, 2017c) from the epochs of strong X-ray flares observed in 2016 August–2017 January and 2016 June–August. One hundred and fifty-three out of 154 curved spectra of Mrk 501 during 2014 March–October showed $a < 2$, and 77 spectra were characterized by $a = 1.39$–1.69 (Kapanadze et al. 2017b). Massaro et al. (2008) reported the value $a = 1.41$ from the *BeppoSAX* observation of Mrk 501 performed on 1997 April 16 (the epoch of the most extreme synchrotron SED peak position discussed in Section 5.1.1). Even more harder 0.3–10 keV spectra with $a = 0.93$–1.27 have been shown by 1ES 0033+595 and H 1515+660 (see Table 11).

Note that the very hard spectra with $a < 1.70$ are rather expected in the framework of hadronic models than within the one-zone SSC scenario (see Mannheim 1993; Shukla et al. 2016), and the higher percentage of such spectra in Mrk 501 and 1ES 1959+650 may hint at the possibly higher hadronic contribution to the jet matter in these HBLs compared to Mrk 421. Nevertheless, 1ES 1959+650 is more prominent with uncorrelated X-ray–VHE variability and "orphan" TeV flares (see Krawczynski et al. 2004; Kapanadze et al. 2016c, 2017c) than our target, and the uncorrelated variability is rather expected in the case of hadronic models (see, e.g., synchrotron proton blazar model; Abdo et al. 2011) than in one-zone SSC scenarios.

As for the power-law spectra, the source exhibited a range of the 0.3–10 keV photon index $\Gamma = 1.75$–2.93. Narrower ranges but harder values were reported for the periods 2005–2008 and 2013 January–May (1.68–2.74 and 1.70–1.76, respectively; Paper I; Kapanadze et al. 2016a). Note that the latter periods were prominent with significantly higher percentage of the power-law spectra: 28% and 13%, respectively, versus 7% in the period presented here. The power-law spectra were even more rarely observed in 2013 November–2015 June (5%; Kapanadze et al. 2017a). A similar, very uneven percentage of the power-law spectra in different epochs was reported for 1ES 1959+650: it amounted to 16% in 2017 January–August against 2% in 2005–2014 and only one occasion in 2015 August–2016 January (Kapanadze et al. 2016b, 2016c, 2017c). We therefore conclude that the physical conditions in HBL jets that are suitable for the establishment of a power-law energy spectrum of the X-ray emitting particles should have an unequal occurrence in different epochs.

In the period presented here, the hardness ratio, calculated from both log-parabolic and power-law spectra, showed an unprecedently broad range with $\Delta HR = 1.37$ and $HR_{max} = 1.47$. However, the source showed a lower percentage of the spectra with $HR \geqslant 1$ than in 2005–2008 (11% versus 26%, although the highest values of HR were practically the same), and such spectra were observed significantly rarely in 2013 January–May and 2013 November–2015 June (8% of all spectra in each period). In 2009–2012, the source followed a "harder-when-brighter" trend during spectral variability that was stronger than in the two aforementioned periods: the correlation coefficient between HR and $F_{0.3-10\,keV}$ amounted to 0.76, while it was equal to 0.53–0.69 in 2005–2009 and 2013–2015. Similar to the very strong 0.3–10 keV flare in 2008 June, the source showed a sub-sample of the spectra that followed an opposite spectral trend, which is unusual for HBL sources (see Paper I). A similar "softer-when-brighter" trend is also observed for the sub-sample from the 2006 June and 2014 January–February observations of our target (Kapanadze et al. 2017a, 2018). Such spectral evolution can be related to the consecutive emergence of soft X-ray components during the flare, resulting in a brightness increase while softening the observed 0.3–10 keV spectrum (see Paper I).

We conclude that Mrk 421 is one of the most extreme HBLs with a very complex, unpredictable timing/spectral variability, exclusively strong X-ray flares in some epochs, and X-ray/HE/VHE flares that sometimes challenge one-zone SSC scenarios. These results, along with the proximity and high X-ray brightness of the source, allowed us to test different models of the MWL emission generation and the nature of instable processes in the innermost AGN area. Therefore, a further densely sampled monitoring of Mrk 421 with *Swift* and other satellite/ground-based instruments in different spectral bands will be very useful for gaining a deep understanding of the AGN phenomenon and blazar physics.

B.K. and L.T. acknowledge the Shota Rustaveli National Science Foundation and Ilia State University for the research grant FR/377/6-290/14. P.R. acknowledges the contract ASI-INAF I/004/11/0. This research has made use of the XRTDAS software, developed under the responsibility of the ASDC, Italy, and the data from the OVRO 40 m monitoring program, which is supported in part by NASA grants NNX08AW31G and NNX11A043G, and NSF grants AST-0808050 and AST-1109911. This research has made use of the VizieR catalogue access tool, CDS, Strasbourg, France. We acknowledge the use of the VHE data from long-term Whipple observations, published in Acciari et al. (2014). UMRAO was supported in part by a series of grants from the NSF, most recently AST 0607523, and by a series of grants from the NASA Fermi Guest Investigator program NNX 09AU16G, NNX10AP16G, NNX11AO13G, and NNX13AP18G. This research has made use of the data obtained through the High Energy Astrophysics Science Archive Research Center Online Service, provided by the NASA/Goddard Space Flight Center Finally, we thank the anonymous referee for very useful suggestions that helped to improve the quality of the paper.

ORCID iDs

B. Kapanadze https://orcid.org/0000-0002-7146-6751
S. Vercellone https://orcid.org/0000-0003-1163-1396
P. Romano https://orcid.org/0000-0003-0258-7469
P. Hughes https://orcid.org/0000-0002-0691-3041
M. Aller https://orcid.org/0000-0003-2483-2103
H. Aller https://orcid.org/0000-0003-1945-1840

References

Abdo, A. A., Ackermann, M., Ajello, M., et al. 2011, ApJ, 736, 131
Acciari, V. A., Aliu, E., Arlen, T., et al. 2009, ApJ, 703, 169
Acciari, V. A., Arlen, T., Aune, T., et al. 2014, Aph, 54, 1
Acero, F., Ackermann, M., Ajello, M., et al. 2015, ApJS, 218, 23
Aharonian, F., Akhperjanian, A. G., Anton, G., et al. 2009, A&A, 502, 749
Ahnen, M. L., Ansoldi, S., Antonelli, L. A., et al. 2016, A&A, 593, 91
Alecsic, J., Ansoldi, S., Antonelli, L. A., et al. 2015a, A&A, 576, 176
Alecsic, J., Ansoldi, S., Antonelli, L. A., et al. 2015b, A&A, 578, 22
Aller, H. D., Aller, M. F., Latimer, G. E., et al. 1985, ApJS, 59, 513
Andruchow, I., Romero, G. E., & Cellone, S. A. 2005, A&A, 442, 57
Atwood, W. B., Abdo, A. A., Ackermann, M., et al. 2009, ApJ, 697, 1071
Balocovic, M., Paneque, D., Madejski, G., et al. 2016, ApJ, 819, 156
Barthelmy, S. D., Barbier, L. M., Cummings, J. R., et al. 2005, SSRv, 120, 143
Blazejowski, M., Blaylock, G., Bond, I. H., et al. 2005, ApJ, 630, 130

Brinkmann, W., Sembay, S., Griffiths, R. G., et al. 2001, A&A, 365, L162
Burrows, D. N., Hill, J. E., Nousek, J. A., et al. 2005, SSRv, 120, 165
Carnerero, M. I., Raiteri, C. M., Villata, M., et al. 2017, MNRAS, 472, 3789
Cui, W. 2004, ApJ, 605, 662
Falomo, R., Pian, E., & Treves, A. 2014, A&ARv, 22, 73
Fossati, G., Buckley, J. H., Bond, I. H., et al. 2008, ApJ, 677, 906
Furniss, A., Noda, K., Boggs, S., et al. 2015, ApJ, 812, 65
Gehrels, N., Chincarini, G, Giommi, P., et al. 2004, ApJ, 611, 1005
Giebels, B., Bloom, E. D., Focke, W., et al. 2002, ApJ, 571, 763
Horan, D., Acciari, V. A., Bradbury, S. M., et al. 2009, ApJ, 695, 596
Howatta, T., Petropoulou, M., Richards, J. L., et al. 2015, MNRAS, 448, 3121
Kalberla, P. M. W., Burton, W. B., Hartmann, D., et al. 2005, A&A, 440, 775
Kapanadze, B., Dorner, D., Romano, P., et al. 2017a, ApJ, 848, 103
Kapanadze, B., Dorner, D., Romano, P., et al. 2017b, MNRAS, 469, 1655
Kapanadze, B., Dorner, D., Vercellone, S., et al. 2016a, ApJ, 831, 102
Kapanadze, B., Dorner, D., Vercellone, S., et al. 2016b, MNRAS, 461, L26
Kapanadze, B., Dorner, D., Vercellone, S., et al. 2017c, MNRAS, 473, 2542
Kapanadze, B., Romano, P., Vercellone, S., et al. 2015, Proc. of the XI Multifrequency Behaviour of High Energy Cosmic Sources Workshop (MULTIF15) (Trieste: SISSA), 56
Kapanadze, B., Romano, P., Vercellone, S., et al. 2016c, MNRAS, 457, 704
Kapanadze, B., Romano, P., Vercellone, S., & Kapanadze, S. 2014, MNRAS, 444, 1077
Kapanadze, B., Vercellone, S., Romano, P., et al. 2018, ApJ, 854, 66
Kapanadze, S., Kapanadze, B., Romano, P., Vercellone, S., & Tabagari, L. 2017d, Ap&SS, 362, 196
Katarzynski, K., Ghisellini, G., Mastichiadis, A., Tavecchio, F., & Maraschi, L. 2006, A&A, 453, 47
Krawczynski, H., Hughes, S. B., Horan, D., et al. 2004, ApJ, 601, 151
Krimm, H., Holland, S. T., Corbet, R. H. D., et al. 2013, ApJ, 209, 14
Levine, A. M., Bradt, H., Cui, W., et al. 1996, ApJL, 469, L33
Macomb, N., Akerlof, C. W., Aller, H. D., et al. 1995, ApJL, 449, L99
Mannheim, K. 1993, A&A, 269, 60
Marscher, A. P. 2014, ApJ, 780, 787
Marscher, A. P., & Gear, W. K. 1985, ApJ, 298, 114
Massaro, E., Perri, M., Giommi, P., & Nesci, R 2004, A&A, 413, 489
Massaro, E., Tramacere, A., Perri, M., Giommi, P., & Tosti, G. 2006, A&A, 448, 861
Massaro, F., Paggi, A., & Cavaliere, A. 2011b, ApJL, 742, L32
Massaro, F., Paggi, A., Elvis, M., & Cavaliere, A. 2011a, ApJ, 739, 73
Massaro, F., Tramacere, A., Cavaliere, A., Perri, M., & Giommi, P. 2008, A&A, 448, 861
Max-Moerbeck, W., Richards, J. L., Hovatta, T., et al. 2014, MNRAS, 445, 437
Mizuno, Y., Pohl, M., Hiemiec, J., et al. 2014, MNRAS, 439, 3490
Padovani, P., & Giommi, P. 1995, ApJ, 444, 567
Perlman, E. S., Madejski, G., Georganopoulos, M., et al. 2005, ApJ, 625, 727
Preziuso, S. 2013, PhD thesis, Univ. Pisa, http://etd.adm.unipi.it/t/etd-10092013-064224/
Punch, M., Akerlof, C. W., Cawley, M. F., et al. 1992, Natur, 358, 477
Ravasio, M., Tagliaferri, G., Ghisellini, G., & Tavecchio, F. 2004, A&A, 424, 841
Rebillot, P. F., Badran, H. M., Blaylock, G., et al. 2006, ApJ, 641, 740
Richards, J. L., Max-Moerbeck, W., Pavlidou, V., et al. 2011, ApJS, 194, 29
Roming, P. W. A., Kennedy, T. E., Mason, K. O., et al. 2005, SSRv, 120, 95
Saito, S., Stawarz, L., Tanaka, Y. T., et al. 2013, ApJL, 766, L11
Shukla, A., Mannheim, K., Chitnis, V. R., et al. 2016, ApJ, 832, 177
Sinha, A., Shukla, A., Saha, L., et al. 2016, A&A, 591, 83
Smith, P. S., Montiel, E., Rightley, S., et al. 2009, arXiv:0912.3621
Sokolov, A., Marscher, A. P., & McHardy, I. M. 2004, ApJ, 613, 725
Steinke, B. 2012, PhD thesis, Tech. Univ. Munich, https://mediatum.ub.tum.de/doc/1097511/document.pdf
Tavecchio, F., Maraschi, L., Pian, E., et al. 2001, ApJ, 554, 725
Tramacere, A., Giommi, P., Perri, M., Verrecchia, F., & Tosti, G. 2009, A&A, 501, 879
Tramacere, A., Massaro, E., & Taylor, A. M. 2011, ApJ, 739, 66
Urry, C. M., & Padovani, P. 1995, PASP, 107, 803
Vaughan, S., Edelson, R., Warwick, R. S., & Uttley, P. 2003, MNRAS, 345, 1271
Virtanen, J. J. P., & Vainio, R. 2005, ApJ, 621, 313
Wierzcholska, A., & Wagner, S. J. 2016, MNRAS, 458, 46